VILNIUS UNIVERSITY
FACULTY OF PHYSICS
LASER RESEARCH CENTER

Austėja Kvedaraitė

DESIGN AND CHARACTERIZATION OF MICROSCALE BEAM EXPANDERS FABRICATED VIA MULTI-PHOTON LITHOGRAPHY

Master thesis

Laser Physics and Optical Technology study program

Student	Austėja Kvedaraitė
Supervisor	Dr. Gordon Zyla
Consultant	Prof. Mangirdas Malinauskas
Reviewer	Dr. Domas Paipulas
Director of the Laser Research Center	Dr. Dalia Kaškelytė
Allowed to defend	2026-05-22

Vilnius 2026

Contents

1. Introduction

Modern optical systems are continuously decreasing in size, driven by the general trend toward miniaturization in integrated optical technologies. Not only do the optical elements scale down but also new methods of shaping the light in nano-/microscale emerge - instead of classical lenses, planar optics and metasurfaces are breaking new ground to further reduce optical system size. [1] As optical components shrink to the micrometer scale, a fundamental challenge emerges – to structure the light in a confined space, for example, directly on a single-mode optical fiber, on laser diodes or for lab-on-a-chip applications, one needs to reach subwavelength feature sizes of optical components. Although lithography techniques can achieve feature sizes of sub-10 nm – as in the case of electron beam lithography [2], which bypasses the optical diffraction limit due to the much shorter wavelength of electrons – they typically rely on complex, high-cost equipment and are usually optimized for nanostructuring flat surfaces under controlled atmospheric conditions. More accessible fabrication approaches such as multi-photon lithography (MPL) are still limited to feature sizes in a few hundred nanometer range, which constrains their applicability for high fidelity beam shaping in strongly confined geometries. [3]

Not only does the technology of choice limit the resolution of microfabrication, but also from a micro-optical perspective, an additional fundamental limitation arises. When structural features of light modulating device are significantly smaller than the optical diffraction limit, the light field cannot resolve them individually and instead responds to their collective, effective optical properties. As a result, the influence of individual features on light field modulation is reduced. Increasing feature sizes enhances their interaction with the optical field but decreases the number of independently addressable elements within a given area, thereby limiting the available degrees of freedom for structuring the light. [4]

Consequently, when high spatial resolution cannot be provided directly within a confined aperture, a common approach is to allow the beam to expand prior to manipulation. Wang et al. [5] demonstrated a dielectric metasurface composed of nanopillars with a height of 600 nm and lateral dimensions of 120 and 335 nm and showed that its effect on beam polarization (depolarization efficiency) improves with increasing incident beam diameter from 10 μm to 200 μm, confirming that larger beam diameters enable more effective polarization control. From a fabrication perspective, increasing the beam diameter relaxes the required feature size of the beam shaping element and allows to have more controllable features to shape light with. However, this strategy comes at the cost of increased system size, as the beam must propagate over several hundreds of micrometers to reach a diameter suitable for conventional beam shaping. For instance, Li et al. [6] fabricated MPL printed metasurfaces integrated on optical fiber facet to create polarization dependent, spatially varying phase. Here the guided fiber mode was intentionally allowed to freely diverge inside a hollow polymer tower to reach beam diameter of ~100 μm before interacting with the metasurface. The total height from the optical fiber facet was ~550 µm. Such heights directly contradict the goal of optical miniaturization and in most cases are impractical for example, in endoscopic imaging in confined anatomy. As emphasized and addressed by Fröch et al. [7], reducing the length of rigid endoscopic probe tips is critical for enabling improved access to otherwise difficult to reach regions of the human body.

This fundamental trade-off between beam size, fabrication resolution, and system compactness motivates the need for advanced beam-engineering approaches that enable light manipulation within tightly confined volumes. Although previous MPL-fabricated beam-shaping systems can increase the beam diameter by allowing the beam to diverge before reaching the active optical element, this strategy increases the total device height and therefore partly counteracts the goal of miniaturization. Therefore, compact refractive microscale beam expanders are investigated in this work as a way to increase the beam diameter within a limited propagation length while maintaining feature sizes compatible with MPL fabrication.

In this context, MPL is employed as the fabrication technique, as it enables sub-micrometer feature resolution without requiring tightly controlled environmental conditions. This makes MPL particularly well suited for fabricating micro-optical components directly on optical substrates, allowing micro-optics to be seamlessly combined with classical optical elements within a single system.

The goal of this work is to design, fabricate and characterize a microscale beam expander with a compact, optimized architecture while still exhibiting effective beam-shaping capabilities over a short propagation distance. For this purpose, transparent organic–inorganic photoresist (SZ2080^{TM}) is used, whose low shrinkage during polymerization, mechanical stability and demonstrated suitability for MPL allow the fabrication of high-fidelity micro-optical structures.

Tasks of the work:

1. To design microscale beam expanders to explore achievable expansion ratios within the constraint of objective working distance (190 µm) while still maintaining high structural fidelity using a high-NA (NA = 1.4) objective.
2. Determine optimal fabrication parameters for the SZ2080^{TM} resin with MPL system used in this work to investigate the achievable quality in fabricating microlenses with MPL.
3. Fabricate beam expanders using MPL and analyze structure and morphology via scanning electron microscope and confocal laser scanning microscope.
4. Test optical characteristics of the fabricated beam expanders at 633 nm.
5. Design, fabricate and test optical characteristics of beam shaping elements – spiral phase plates.
6. Fabricate, characterize and test optical performance of integrated beam-shaping micro-optical device.

2. Literature overview

2.1 Multiphoton lithography (MPL) and photosensitive materials

MPL is an additive or subtractive manufacturing technique, also referred to as laser direct writing (LDW), which enables creation of high precision 3D micro/nanoscale structures with features exceeding the diffraction limit. In additive MPL, the interaction of matter with light results in the polymerization of the monomers/oligomers of the material. Specifically, upon radiation, through radical photopolymerization mechanisms, the prepolymer formed cross-linked network of polymer chains resulting in an insoluble (under the development conditions) and mechanically stable microstructures.

Organic or hybrid organic-inorganic resins are usually used as the fabrication media for the MPL process. The main requirements for resin materials include high optical transparency at the fabrication wavelength to minimize linear absorption, an absorption peak suitable for multiphoton excitation, and good solubility of all components in the monomers being used. Photoinitiators (PIs) are often added into the resin to undergo multiphoton absorption and generate radicals that initiate cross-linking reactions. Formation of radicals relies on nonlinear optical phenomenon called multiphoton absorption (MPA). MPA is defined as nonlinear response to incident electric field and is the ability of a material to absorb more than one photon simultaneously via virtual energy levels. (Fig. 1)

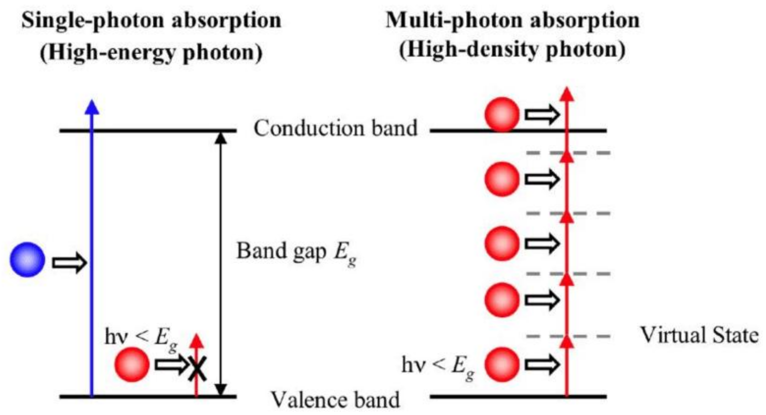

Fig. 1 Electron excitation process in materials by single and multiphoton absorption. From [8].

For this process to occur, high intensities in the order of TW/cm^2 are required. Assuming Gaussian spatial and temporal pulse profiles the peak intensity of the laser radiation at the focus position can be calculated as:

$$I_p = \frac{2PT}{f\omega^2\pi\tau}, \quad (1)$$

where P – average laser power, T – objective transmission, f – laser pulse repetition rate, ω – radius of the beam and τ – pulse duration. According to the equation, to induce nonlinear absorption for MPL, ultrashort laser pulses together with tight focusing should be used as it temporally and spatially increases the density of photons and raises the probability of multiphoton absorption in a medium.

Upon MPA, in case of radical polymerization, the medium undergoes 3 steps of cross-linking reaction: initiation, when photosensitive molecules are excited by the incident light and start to interact with monomers; propagation when the polymer chain elongates rapidly by the interaction of free bonds with unreacted monomers; and termination, when radical activity ceases through recombination, disproportionation, or primary radical termination, resulting in non-reactive polymer chains. (*Table 1*)

Table 1. Equations of radical polymerization. From [9].

Polymerization steps	**Radical polymerization**
Photolysis	$PI \xrightarrow{h\nu} PI^* \rightarrow R^*$
Initiation	$R^* + M \rightarrow RM^*$
Propagation	$RM^* \rightarrow RMM^* \rightarrow \ldots \rightarrow RM_n^*$
Termination	**Primary radical termination:** $RM_n^* + R^* \rightarrow RM_nR$
	Recombination: $RM_n^* + RM_m^* \rightarrow RM_{n+m}R$
	Disproportionation: $RM_n^* + RM_m^* \rightarrow RM_n + RM_m$

There is a possibility to initiate polymerization without PI, by MPA or ionization mechanisms. In this process, several photons can be absorbed quasi-simultaneously, providing enough energy to ionize the resin matrix itself. Once ionization occurs, free electrons and radical ions are generated. These species can initiate polymerization. For this process to occur there is a need for higher intensities, reaching ~10^{13}–10^{14} W/cm^2 (tens or hundreds of TW/cm^2). Nevertheless, not all monomer systems are well suited for initiator-free photo-cross-linking. In vinyl-based resins, the relatively high bond dissociation energy of the C=C group (~4.5 eV) makes direct radical generation inefficient, requiring significantly higher excitation intensities. [9]

The elimination of synthetic photoinitiators is attractive because PIs can be toxic, and PI-free formulations can therefore support the development of more biocompatible photoresists. For example, plant-derived acrylate systems have been demonstrated to polymerize under ultrashort-pulse LDW without any PI, where multiphoton absorption and avalanche-induced cross-linking enabled feature sizes down to ~1 µm and a reported throughput of ~6900 voxels/s. [10]

Moving further from polymerization mechanisms, the fundamental building block of MPL is voxel – localized volume of cured resin formed at the laser focal spot where the exposure dose exceeds the polymerization threshold. The existence of this threshold enables spatial confinement of polymerization in volume below the diffraction-limited focal spot. The lateral laser diffraction limited focal spot diameter can be expressed by the following equation:

$$2\omega = \frac{1.22\,\lambda}{NA}, \tag{2}$$

where λ – wavelength, *NA* – numerical aperture of the objective.

The axial size of the focal region can be expressed as twice the Rayleigh length:

$$2z_R = \frac{2\pi\omega^2}{\lambda} \tag{3}$$

where ω – radius of lateral focal spot, λ – wavelength. [11] Only a portion of the diffraction-limited focal volume exceeds the polymerization threshold for a given material. As a result, the formed voxels can be significantly smaller than the focal volume of the laser beam. This behavior depends on laser intensities as schematically depicted in Figure 2.

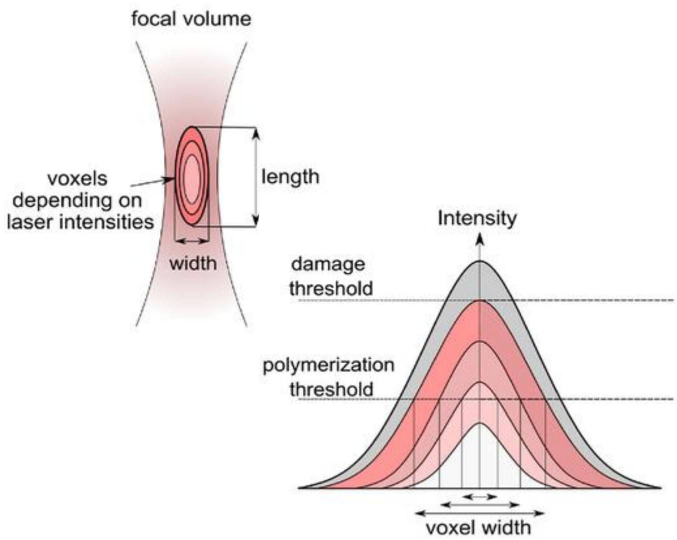

Fig. 2 Polymerization occurs in small building blocks – voxels, which dimensions depend on laser intensities. Adapted from [12].

As the applied intensity is increased above the polymerization threshold, the voxel dimensions grow because a larger fraction of the focal intensity distribution exceeds the threshold. The polymerized volume (voxel) is typically ellipsoidal – elongated along axial dimension, because axially the intensity decays more slowly over the Rayleigh range. [9]

Light intensity cannot be increased infinitely, MPL is a threshold-dependent process and occurs at certain radiation intensity range – dynamic fabrication window (DFW). This window is defined by the lower polymerization threshold and the upper optical damage threshold of the material, within which stable and controllable fabrication is possible. Operating near the lower edge of the window only the very center of the focal volume of a laser beam exceeds the excitation threshold, producing the smallest voxels. As intensity increases within the window, the space within the focused laser beam where the laser intensity has the same value everywhere, expands, leading to predictable lateral and axial voxel growth. Once the upper boundary of the DFW is crossed, voxel growth becomes erratic: bubbles, voids, and material removal appear. [13]

2.2 MPL for optics and light manipulation at the microscale

MPL offers several key advantages, including maskless and fully 3D fabrication yielding smooth surfaces, as well as a wide range of transparent photosensitive resins and diverse post-processing strategies such as calcination, which removes the organic fraction and converts printed structures into glassy or ceramic-like materials with enhanced mechanical strength and laser-induced damage threshold [14] or coating approaches that can be employed to further improve optical transmission [15]. Together, these capabilities open a broad and versatile field of micro-optical devices fabricated by MPL including microlenses, diffractive optical elements, metalenses or other beam shaping structures.

An electromagnetic wave can be described by its electric field as

$$E(x, y, z, t) = A(x, y, z)\cos\big(kz - \omega t + \phi(x, y, z)\big), \tag{4}$$

where A – amplitude, k – wave number, ω – angular frequency, and ϕ – phase. [16] From this expression, it is clear that light can be modulated by changing its amplitude or intensity, polarization, frequency, phase or wavefront. The latter could be modulated by spiral phase plates (SPPs), which can also be fabricated by MPL. SPPs introduce a spatially varying phase delay around the optical axis, transforming an initially planar wavefront into a helical wavefront. (Fig. 3)

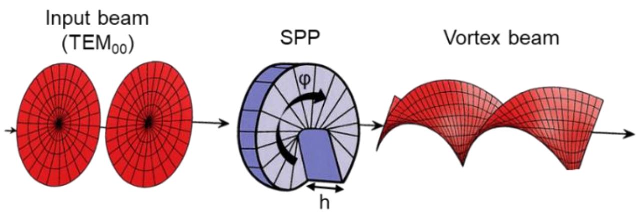

Fig. 3 Schematic illustration of optical vortex beam generation using SPP. Adapted from [17]

The phase of light describes where the electromagnetic wave is within its oscillation cycle, and one complete cycle corresponds to a phase change of 2π. A phase delay of 2π, 4π, or 6π means that the wave has been delayed by one, two, or three full periods. However, because the optical field is periodic, these full-period delays are equivalent in phase – the wave after an integer number of delays returns to the same point in its oscillation cycle. In an SPP, the phase delay is introduced by changing the height of the structure: a thicker region gives light a longer optical path and therefore a larger phase delay. The phase delay caused by a height (h) is

$$\Delta\phi = \frac{2\pi}{\lambda}(n - n_0)h, \tag{5}$$

where λ – wavelength, n – refractive index of the SPP material, and n_0 – refractive index of the surrounding medium (usually air). Therefore, the height needed for one full 2π phase delay is

$$h_{2\pi} = \frac{\lambda}{n - n_0}. \tag{6}$$

This formula shows that the required height depends directly on the wavelength and on the refractive-index contrast. A larger refractive-index contrast means a smaller physical height is needed to obtain the same phase delay. For an SPP, the desired phase changes with the azimuthal angle φ, and is described by

$$\phi(\varphi) = l\varphi, \tag{7}$$

where l – topological charge. The topological charge tells how many full 2π phase windings occur in one full rotation around the optical axis. For example, l = 1 means one 2π phase winding, l = 2 means two windings, or 4π total phase change. Moving to fabrication of SPPs, for l = 2, the required 4π delay can be produced either by making one structure with twice the 2π height,

$$h_{4\pi} = 2h_{2\pi}, \tag{8}$$

or by making two repeated 0 to 2π ramps around the plate. These give the same phase because after each 2π ramp the phase returns to an equivalent value. Thus, the maximum height determines the phase depth, while the number of repeated ramps in a SPP determines the topological charge. [18], [19]

Although phase delays of 2π, 4π, and 6π correspond to the same point in the electromagnetic wave oscillation cycle, SPPs with l = 1, l = 2, and l = 3 do not generate the same beam intensity distribution. For higher topological charges, the phase changes more rapidly (the same angular step corresponds to greater phase change) around the optical axis. In an l = 1 beam, the phase completes one full 2π cycle during one rotation around the center, while in an l = 2 or l = 3 beam it completes two or three cycles over the same angular distance. This means that in higher order topological charges, close to the axis, opposite phases are closer together in space. During propagation, these fields overlap and destructively interfere, keeping the central intensity low over a wider area. Destructive interference becomes less dominant further from the center where the same phase variation is spread over a larger circumference therefore intensity can increase. As a result, higher $|l|$ vortex beams usually have a larger dark core and more diverged intensity ring. (Fig. 4)

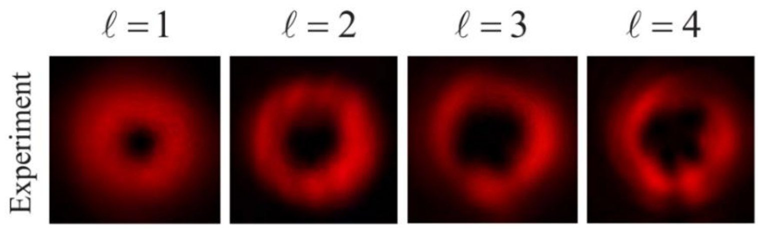

Fig. 4 Far field intensity pattern when a focused Gaussian beam 633 nm incident onto a SPP radius 40 μm located in the focal plane of the incident beam with different integer topological charges. The distance between the SPP plane and the observation plane is a few tens of the Rayleigh distance. [20]

Negative topological charges are also possible. A positive l and a negative l have the same number of phase turns, but the handedness of the helix is opposite. For example, $l = +3$ and $l = -3$ both contain one full 6π phase turn around the optical axis, but the phase increases in opposite angular direction and produces vortex beam with opposite orbital angular momentum (Fig. 5).

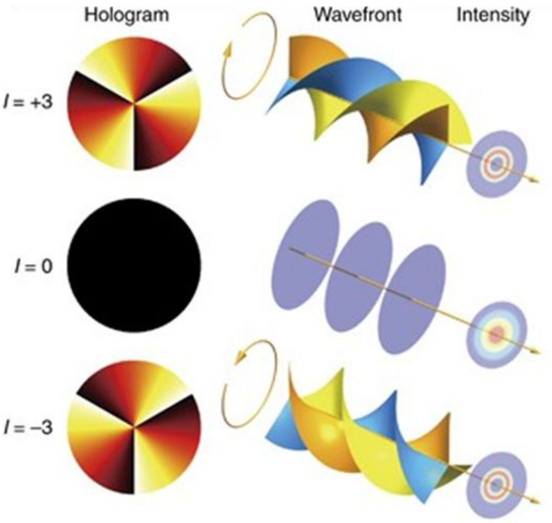

Fig. 5 Illustration of the optical vortex holograms with topological charge $l = 3$ and $l = -3$ and the corresponding optical helical phase wavefronts. Adapted from [21].

Despite its versatility, MPL has several practical limitations for micro-optics. One clear limitation is resolution. Though MPL breaks the diffraction limit, it still cannot reach the single-nanometer precision. That becomes clear in such applications where it is being attempted to modulate light at the facet of optical fiber. Here emitted mode is tightly confined and exhibits steep phase and amplitude gradients. Accurately modulating such a field would require sub-100 nm lateral resolution and extremely fine axial control, which remains challenging for MPL under practical fabrication conditions. As a result, beam-shaping elements fabricated by MPL are not placed directly at the fiber output plane, but instead positioned at some distance where the beam has naturally diverged and it is easier to structure beam's spatial phase profile. (Fig. 6)

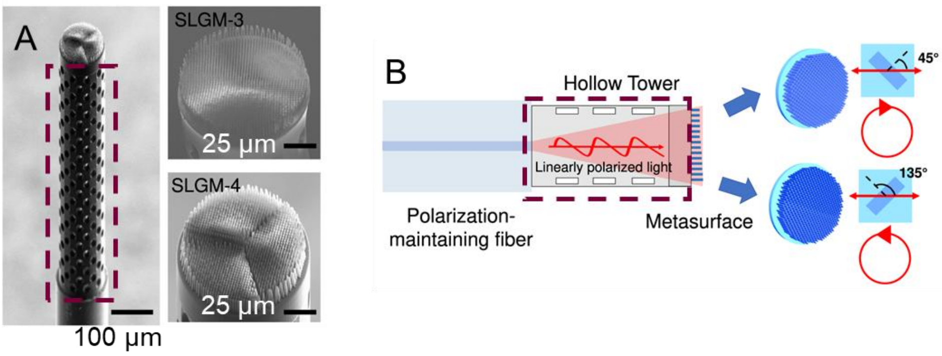

Fig. 6 A – scanning electron microscopy images of fabricated metafibers. B – schematic illustration of metafibers used for light manipulation. Dashed lines show hollow tower support. Adapted from [6].

To date, there are not many approaches that realize beam expanders using MPL-fabricated micro-optics. Instead, MPL printed micro-optics predominantly target imaging or beam-shaping functionalities. [22], [23], [24] But attention is drawn to further minimizing already miniature optical systems. This miniaturization is highly significant for medical applications, particularly endoscopy, where light must be guided through compact spaces and the rigid imaging optics on endoscopic probes limit their functionality. Previous studies have investigated replacement of conventional graded-index lenses with meta-optics, achieving rigid tip length reduction of approximately 33%. However, such meta-optical imaging approaches rely on specific optical responses that require careful design, calibration, and computational reconstruction to retrieve image information, which can complicate real-time operation. [7] In contrast, MPL-fabricated micro-optical lenses provide direct, real optical functionality through refractive, multi-surface designs that can be modeled with already established optical ray tracing tools and operate without excessive computational image reconstruction. [25]

2.3 Classical type beam expanders (BE) and perspectives enabled by MPL

To address the issue of effective light modulation in a confined space, beam expanders could be used to increase beam diameter before further optical processing. Classical beam expanders are afocal two-lens telescopic systems that enlarge a beam's diameter and thus reduce divergence. The expansion factor (M) is determined by the ratio of the focal lengths of the optical elements:

$$M = \frac{f_2}{f1}, \tag{9}$$

where f_1, f_2 – focal length of first and second lens in a beam expander, respectively.

There are two types of classical type BEs: Keplerian and Galilean designs. (Fig. 7) In Keplerian design, two positive lenses are separated by the sum of their focal lengths. The first positive (convex) lens focuses the incoming beam to intermediate focus, while the second convex lens re-collimates it at a larger diameter. In contrast, a Galilean expander pairs a negative (concave) lens with a convex lens, spaced by the difference in focal lengths, resulting in a shorter, non-inverting system. The Galilean configuration offers key advantages: it is more compact and has no internal focus (which might become critical when dealing with higher light intensities). These benefits have made Galilean beam expanders popular in situations where overall system size and beam quality are critical. [26]

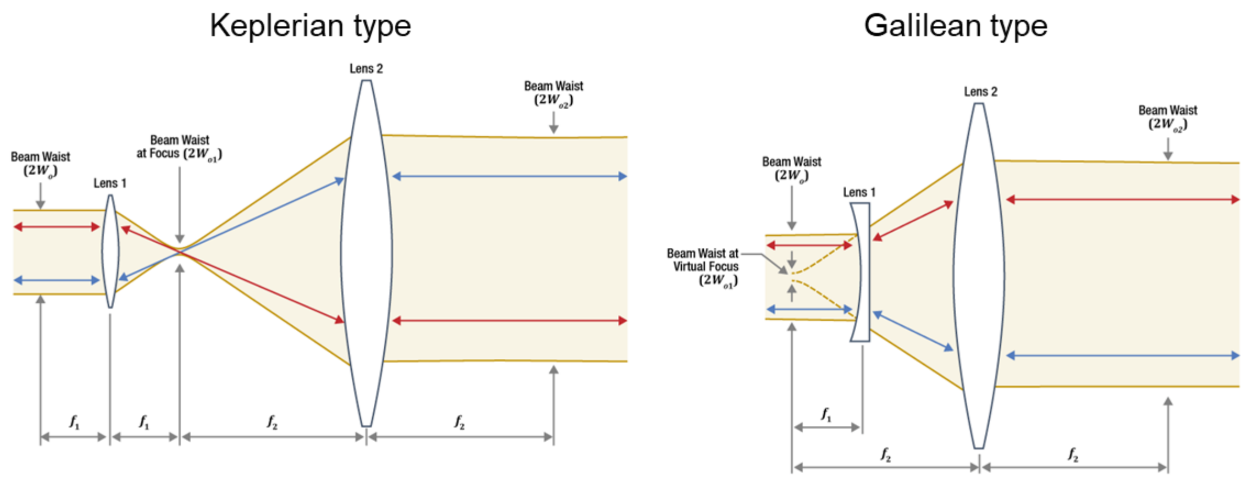

Fig. 7 Classical types of BEs. Adapted from [26].

Conventional macroscale designs treat beam expansion and aberration correction as separate functions, implemented by distinct optical components placed sequentially along the beam path. This applies to micro-optics as well, as it was shown that increasing the number of refractive interfaces (multi-lenses) distributes optical power across multiple surfaces and provides additional degrees of freedom that allow aberrations such as coma, astigmatism, field curvature, and distortion to be balanced through surface geometry and spacing. [25] On the other hand, free-form optical design, enabled by MPL, allows designs with non-rotationally symmetric surface geometries. Therefore, beam expanders fabricated via MPL could be realized as compact elements in which beam expansion and aberration correction are integrated within a single 3D unit. For example, using MPL, spherical aberration correction can be integrated directly into the beam expanding element by designing aspheric geometry that imposes an opposite phase error. As it is already shown that MPL-fabricated elements can controllably and locally affect phase. [27] If made in such way that marginal rays accumulate a compensating phase delay, flattening the output wavefront, this would allow to have beam expansion and spherical aberration correction achieved simultaneously within a single optical element.

Furthermore, chromatic aberration arises from the wavelength dependence of a material's refractive index, which causes different spectral components of light to experience different optical path lengths. As a result, a lens focuses different wavelengths at different axial or lateral positions. In conventional optics, chromatic aberration is typically mitigated through achromatic designs, most commonly by combining materials with different dispersion properties such as crown and flint glasses doublets to balance the opposite chromatic focal shifts of materials with low and high Abbe numbers. [28] Research on multi-material MPL suggests the possibility of spatially differentiating regions within the same structure by sequentially writing different resins with distinct optical properties. [29], [30] This could simulate the functional role of crown and flint glasses combinations at the microscale. Although such achromatic, multi-material micro-optics designs produced by MPL are not widespread, multi-material MPL developments give prospects that combining free-form geometry with controlled choice of material could offer a route to compensate aberrations in compact micro-optical elements.

2.4 Predicting light at microscale

The prediction of optical performance of a lens system could be approached from different levels of physical approximation. The hierarchy begins with geometrical optics, then goes to scalar wave optical models and finally to full vector electromagnetic simulations. The suitable model depends mainly on the relationship between the wavelength and the feature size of the optical component also on the numerical aperture of the component, the coherence of illumination, and whether polarization effects are important.

Geometrical optics, also called ray optics, is the simplest and fastest method for simulating light propagation. In this model, light is represented by rays that travel through an optical system according to Fermat's principle, eikonal equation, Snell's law. Fermat's principle states that in a region of constant refractive index, light travels between two points along the path that takes the least time. And how ray travels that path is governed by eikonal equation:

$$[\nabla L(r)]^2 = n^2(r), \tag{10}$$

where $n(r)$ is the refractive index at position r, $L(r)$ is the optical path length and $\nabla L(r)$ describes how this optical path length changes with position. This means that for each physical distance travelled, the optical path length increases by n times that distance. And the operator ∇ here suggests that $L(r)$ value is a function of every x, y, z point in space, therefore ∇L gives a vector which tells the ray direction. If the wave comes from a point source, then L forms spherical wavefronts, and ∇L points radially outward (perpendicular to the wavefront), so rays spread away from the source. If the ray hits a lens surface, the new direction is determined by Snell's law at that surface. After that, the new wavefront shape is changed, so ∇L points in the new refracted direction, but always perpendicular to wavefront. Snell's law describes refraction when light goes from one medium to another and predicts critical angle at which light travelling from higher refractive index medium into a lower refractive index medium forms total internal reflection.

This approximation is highly useful for first-order optical design, lens layout, paraxial analysis, pupil placement, chief and marginal ray analysis, and preliminary aberration estimation. Standard optical design therefore often begins with ray tracing, because it gives a direct and computationally efficient description of how light travels through optical components. [31] However, ray optics cannot describe diffraction, interference, polarization, or scattering from surface features comparable to the wavelength. [16], [32]

Micro-optics often lie in a transition regime – their overall shape may be large enough for ray tracing, but, for example local features of diffractive optical elements, metasurfaces require optical field to be treated as wave. Lindlein [33] similarly emphasizes this for microlens arrays, where a single aperture stop or exit pupil may not describe the optical system because each microlens has its own small aperture, neighboring lens may clip or diffract different parts of the field, and different rays may pass through different local optical paths.

A common next step in the hierarchy of modelling is scalar wave optics. Here light is no longer represented only by ray trajectories, but by a complex scalar field *u(r)*, which contains both amplitude and phase (amplitude is no longer a constant as it was in ray optics). The field is still approximated and described by one complex value at each point in space, rather than by the full vector electric field. Scalar wave optics can describe diffraction and interference, but it still neglects polarization. The governing equation is the scalar Helmholtz equation:

$$[\nabla \cdot \nabla + (nk_0)^2]u(r) = 0, \tag{11}$$

where *u(r)* is the complex optical field, *n* is the refractive index, and $k_0 = 2\pi/\lambda_0$ is the free-space wavenumber. Unlike geometrical optics, which follows ray paths, scalar wave optics propagates the complex field itself. The intensity is then obtained from the field as $I(r) \propto | u(r) |^2$, while in ray optics intensity is represented as the density of rays in a given area. The main new physical effects included in scalar wave optics are phase, diffraction, and interference. Interference appears because overlapping fields are added as complex amplitudes before intensity is calculated. When the summed field is squared to obtain intensity, the result contains an additional term that depends on the phase difference between the waves. For example, two fields, $u_1 = A_1 e^{i\phi_1}$ and $u_2 = A_2 e^{i\phi_2}$, the intensity is $I = | u_1 + u_2 |^2 = A_1^2 + A_2^2 + 2A_1A_2cos(\phi_1 - \phi_2)$. The last term, $2A_1A_2cos(\phi_1 - \phi_2)$, is the interference contribution – it increases the intensity when the waves are in phase and decreases it when they are out of phase. Therefore, scalar wave optics can predict diffraction fringes, Airy patterns, coherent image formation, and wavelength-dependent resolution, while ray optics cannot describe these effects directly.

Scalar wave propagation can be calculated using Fresnel diffraction, Fraunhofer diffraction, Rayleigh-Sommerfeld diffraction, or the angular spectrum method. These methods are different ways of solving or approximating the scalar Helmholtz equation. For example, Rayleigh-Sommerfeld diffraction treats every single point in the starting aperture as a tiny source of spherical ripples. It calculates how every single ripple travels by applying a spherical wave formula and adds them at the image plane. It is highly accurate but mathematically heavy to compute. In the angular spectrum method, instead of looking at a plethora of spherical ripples, it looks at the whole starting wave and breaks it down via Fourier transform into a set of flat, straight waves traveling at different angles. Other methods, Fresnel and Fraunhofer diffraction, are mathematical approximations related to the more general Rayleigh-Sommerfeld formulation. Fresnel diffraction is used for finite-distance propagation under the paraxial approximation, meaning that the field mainly propagates at small angles relative to the optical axis. Fraunhofer diffraction is an approximation for the extreme far-field. It assumes that the waves arrive flat, which conveniently simplifies the entire propagation equation to a simple 2D Fourier transform.

However, scalar wave optics is still an approximation. Since it represents light by a single scalar field, it does not fully include polarization, longitudinal field components, or coupling between electric-field components at interfaces. Therefore, scalar wave optics is suitable when diffraction and interference are important, but polarization is not a dominant factor. If the system contains high numerical aperture focusing, gratings, metasurfaces, subwavelength structures, steep incidence angles, or polarization sensitive elements, full vector electromagnetic simulation may be required. In these cases, the direction of the electric field becomes important because light polarized parallel or perpendicular to an interface can be reflected, transmitted, or phase-shifted by different amounts. [34]

The most complete model is vector wave optics, based on Maxwell's equations. Here light is represented by coupled electric and magnetic fields rather than by rays or a single scalar amplitude. From Maxwell's equations, one can derive wave equations for the electric and magnetic fields. In a simple source-free, homogeneous, nonmagnetic medium, where ε (electric permittivity, describes how strongly a material responds to an electric field) and μ (magnetic permeability, describes how strongly a material responds to a magnetic field) are constant and $\sigma = 0$ (σ – electrical conductivity – describes how easily electric charge can move through the material), the electric-field wave equation can be written in simplified form as

$$\nabla^2 \boldsymbol{E} - \frac{n^2}{c^2}\frac{\partial^2 \boldsymbol{E}}{\partial t^2} = 0, \tag{12}$$

where c – speed of light in vacuum, t – time, and n – refractive index of the medium. For time-harmonic fields this leads to a vector Helmholtz-type equation,

$$\nabla^2 \boldsymbol{E} + n^2 k_0^2 \boldsymbol{E} = 0. \tag{13}$$

The important difference from scalar wave optics is that $\boldsymbol{E}$ is a vector field, meaning that the simulation must describe all field components E_x, E_y, E_z, not only one scalar amplitude *u(r).* Therefore, vector wave optics can directly describe polarization state, longitudinal field components, and coupling between field components at interfaces. [16], [32], [35]

Full vector wave simulations are computationally heavy because they resolve the electromagnetic field throughout a 3D simulation volume with fine spatial sampling. As highlighted by Wende et al. [34] rigorous methods can be impractical, potentially requiring hundreds of years to simulate structures only a few hundred micrometers in size. While scalar methods offer a faster alternative, they fail to account for polarization, which is critical in high-NA optics. To bridge this gap, the Fast Polarized Wave Propagation Method (FPWPM) is proposed as a high efficiency trade-off, significantly reducing hardware requirements while retaining essential vector information. The authors prove the validity of this method in Figure 8 by simulating high-NA (0.72) microlens. The focal-plane intensity distributions produced by FPWPM (panels e, f) show good match with the rigorous Richards-Wolf integral, which is vector diffraction method used to calculate tightly focused electromagnetic fields in high-NA systems (panels g, h). Conversely, the scalar WPM results (panel i) deviate sharply, proving that simplified scalar methods that neglect polarization are insufficient for high-NA systems and newly developed FPWPM avoids this error. However, this gain in computational speed comes with trade-offs. The FPWPM achieves its efficiency by omitting backward-propagating waves (reflections) and can lose accuracy at extremely steep angles or with TM-polarized light. Therefore, it is important to understand which approximations are acceptable and which effects must be retained for reliable light prediction in a specific design.

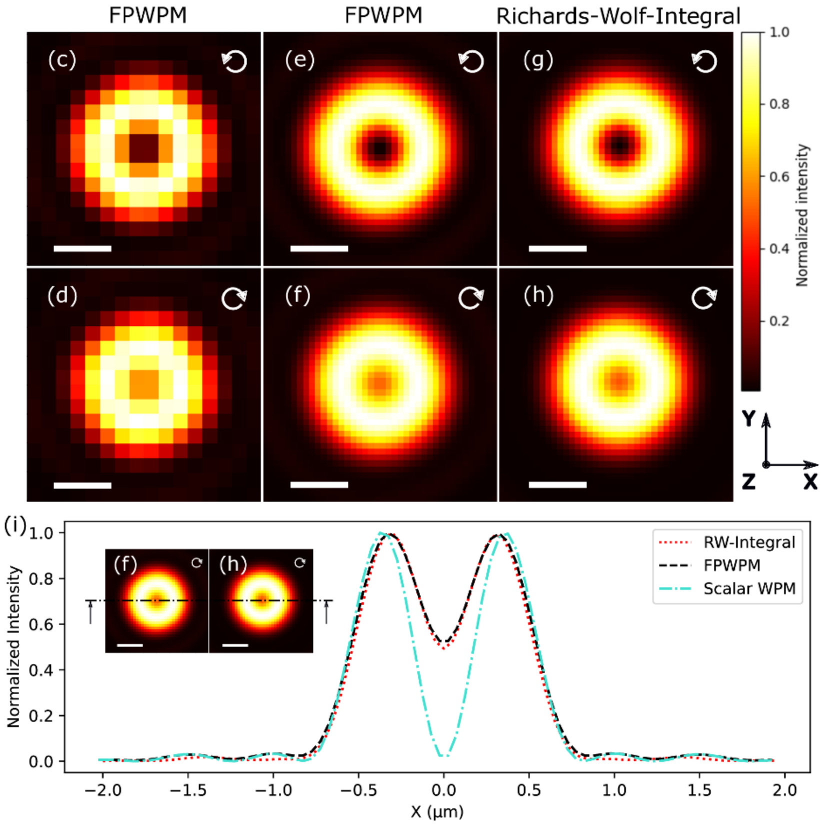

Fig. 8 Simulation of electric field propagation through a microlens for normal plane wave incidence at λ = 0.635 µm. c-d – simulated intensity in the focal plane of the microlens. The handedness of the circular polarization used in the simulations is indicated in the upper right corner. Scale bars: 0.5µm. c+d FPWPM, dx = dy = dz = 0.127 µm. e + f FPWPM, dx = dy = dz = 0.05 µm. g +h RW-Integral, dx = dy = 0.05 µm. i – comparison of cross sections through foci in (f) and (h) and the focus obtained with the scalar WPM. Adapted from [34]

3. Materials and methods

3.1 Sample preparation and development

The photoresist used in this work is SZ2080^{TM}. It is a hybrid photoresist formulation consisting of organic and inorganic components. The organic monomers are MAPTMS ((3-methacryloyloxypropyl) trimethoxysilane) and methacrylic acid (MAA). The inorganic precursor is zirconium n-propoxide (ZPO, 70% in propanol), which, together with hydrolyzed MAPTMS, forms an inorganic Zr–O network within the polymer matrix. The incorporation of ZPO reduces shrinkage and improves structural stability. [36] The molar ratio of MAPTMS:ZPO:MAA is 8:2:1. As a photoinitiator, BIS (7-diethylamino-3-thenoylcoumarin) was added at a concentration of 1 wt% relative to the total monomer content. The resulting SZ2080^{TM} hybrid material exhibits high transparency in the infrared spectral range, and therefore polymerization with 1030 nm is governed by multiphoton absorption (Fig. 9).

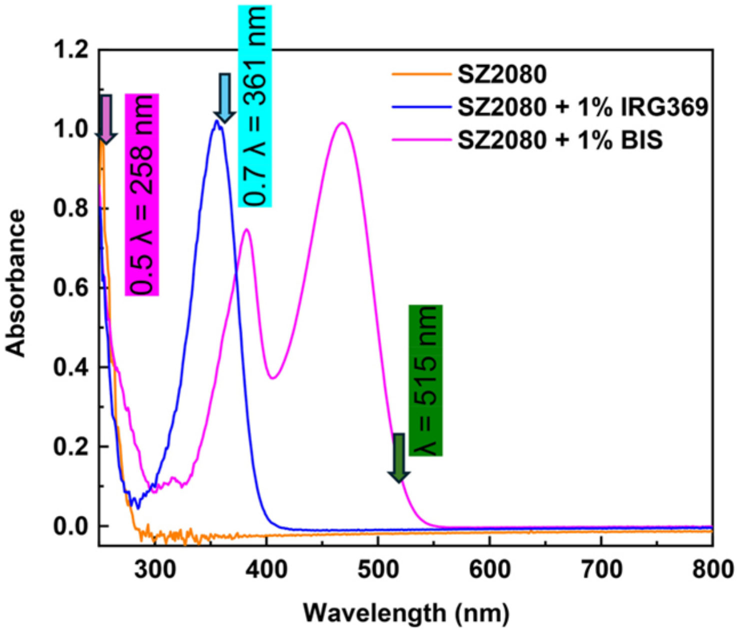

Fig. 9 UV-Vis absorption spectra of SZ2080^{TM} with and without PI. Adapted from [37].

For sample preparation a drop of resin was placed on borosilicate glass coverslip (thickness 170 µm ± 5 µm) and left in a vacuum chamber (~0.4 bar pressure) for at least 2 days to further promote sol–gel condensation and avoid oxygen residues in the prepolymer, which can cause photopolymerization quenching and poor polymer rigidity after chemical development. Prepolymer drops were kept in an environment preventing the sample from light exposure before the fabrication.

After laser fabrication, the samples were developed for 30-60 minutes using isopropanol (propan-2-ol) or for 10-15 minutes using 4-methyl-2-pentanone to remove unpolymerized material and reveal structures.

3.2 MPL setup

The microfabrication setup consists of femtosecond solid state laser "Pharos" (Light Conversion, Lithuania): the active medium is a Yb:KGW crystal, central wavelength of the fundamental irradiation is λ=1030 nm. The laser generates pulses of τ < 300 fs duration. Used repetition rate 100 kHz. Laser beam is guided through home-built setup, which includes attenuator to have full control over laser power exposed to the material.

Then the beam is directed to beam expander unit, galvanometer scanner system (ScanLab) and translated via 4f optical relay to the objective, where tight focusing on the sample is achieved. The objective and the focusing position on the sample is adjusted with z translational stage (Aerotech) and sample's position is adjusted with x and y translational stage (Aerotech). The fabrication process is observed in real time using CMOS camera and bottom LED lighting. (Fig. 10)

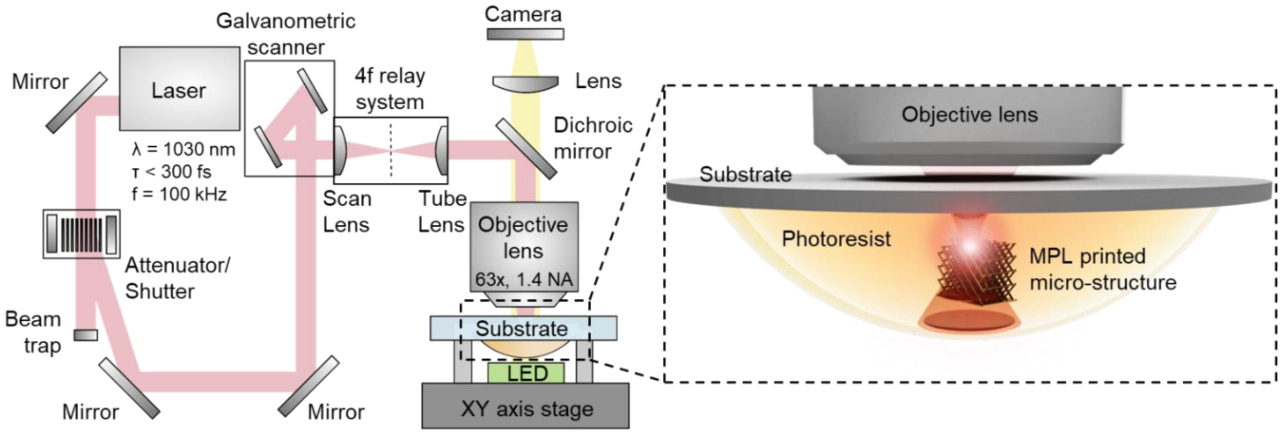

Fig. 10 Typical MPL microfabrication setup.

For all fabrications, 1030 nm wavelength laser beam was focused using Zeiss 63x, 1.4 NA plan-apochromat oil immersion objective (190 μm working distance, 25 mm field of view at the image plane). Diffraction-limited focal spot size according to equation (2) and (3) is ~0.90 μm lateral diameter and ~1.23 μm axial length having NA = 1.4 and λ = 1030 nm.

Prepared models were exported as *.stl* files, and additional supporting structures were added via Autodesk Fusion 360 software. In 3DPoli 6.12 Compiler program, *.stl* files were imported, and the following parameters of the fabrication were determined: model orientation, laser scanning velocity, average fabrication power, model slicing and hatching values, type of scanning grid. Slicing (S) determines an interspacing between a set of layers in the model sorted along z axis. Each sliced plane is perpendicular to z and parallel to xy axes. The transition from adjacent sliced planes refers to the objective movement along z axis. Hatching (H) is a distance between parallel laser scanning lines in each layer. (Fig. 11) Laser beam scanning along hatching lines corresponds to the movement of galvanometric mirrors. 3DPoli 6.12 Fabrication program was used to manually control MPL system.

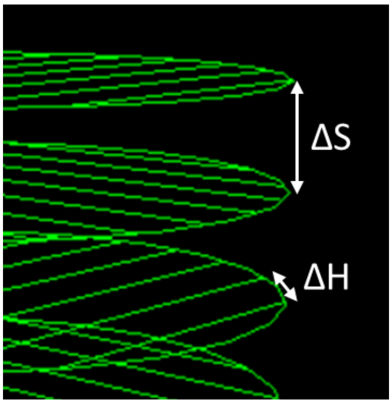

Fig. 11 Slicing and hatching of the *.stl* model at 3DPoli software.

3.3 Structural and morphological analysis tools

Initial inspection of samples was performed using an inverted optical microscope Olympus BX51. Assessment of finer details of a structure was conducted using scanning electron microscopes (HITACHI TM-1000 and TS Prisma E). For scanning electron microscopy (SEM) imaging samples were coated with a 5 nm layer of Ag or Au using Quorum Q150R S sputtering system to reduce surface charging and improve electron conductivity, thus enhancing image quality during SEM imaging.

To evaluate and further improve the precision in writing, surface profile analysis was performed by confocal laser scanning microscope OLYMPUS Lext OLS5100. It has 2 types of optical systems: color imaging optical system and laser confocal optical system. The color imaging optical system uses white LED light source and CMOS image sensor. Since the focal depth of the color imaging optical system is deeper than that of the laser confocal optical system, it was used for searching for the measurement position of the sample. The laser confocal optical system acquires the confocal image using the semiconductor laser light source (wavelength: 405 nm) and the high sensitivity detector (photomultiplier). Laser confocal optical system has shallow focal depth, so it was used for measuring the sample's surface. Measurement is performed by collecting reflected or scattered light from the sample by the same objective through which light was transmitted. Confocal microscope has a circular pinhole (Fig. 12) ensuring that only light originating from the focal plane reaches the detector. The detected signal intensity is recorded as a function of XY scan position and forms a confocal image.

For height (z) measurement, the system changes the focal position stepwise along the z direction and acquires multiple confocal images at different focus depths. For each pixel, the system analyzes the relationship between detected intensity and focal position. The z position where the signal is strongest indicates the location of the sample's surface for that pixel, and assembling these positions over the entire scan produces surface height map. If needed, received images were digitally postprocessed by correcting the tilt of the substrate and removing noise, arising at steep angles, where reflected light does not fully pass through the pinhole, increasing height uncertainty and causing incorrect height values at some pixels. By applying spike removal, extreme outlier pixel values were removed.

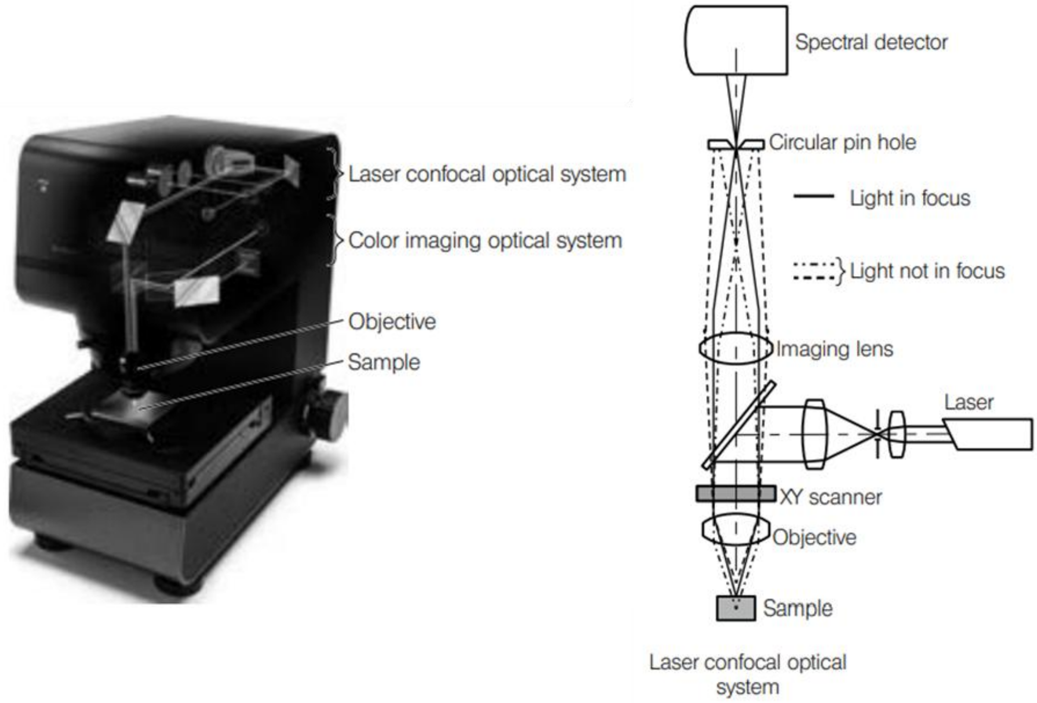

Fig. 12 Configuration of confocal laser scanning microscope OLS5100. Adapted from [38]**.**

3.4 Optical performance testing setup

To assess the transparency and optical performance of the MPL-printed structures at 633 nm, the optical setup shown in Figure 13 was used. In all cases MPL printed microstructures were facing upwards and light was focused on to the sample through Objective 1 and collected by Objective 2. Objectives could be moved up and down and sample stage allowed movement in XY directions. The absolute transmission of each printed structure was determined from the ratio of the photodiode signals, PD2/PD1, where PD1 monitored the incident beam and PD2 measured the transmitted beam. To account for fluctuations in laser power and optical losses from the substrate, the PD2/PD1 ratio measured through the printed structure was normalized to the corresponding ratio measured through a nearby unstructured region of the glass substrate. Therefore, the reported transmission values represent the transmission of the printed structures relative to the glass substrate. Data acquisition was performed using a custom algorithm written by Dominykas Dapšys. For each measurement point, the photodiode signals were recorded over a five-second interval, and the average, minimum, and maximum values were stored. This allowed short-term fluctuations in the laser output and detector signals to be included in the analysis. For optical performance characterization, the transmitted light was directed to a CCD camera (mvBlueFox 223C, Matrix Vision) through the collection optics enabling evaluation of the beam profile and focusing behavior after propagation through the printed structures.

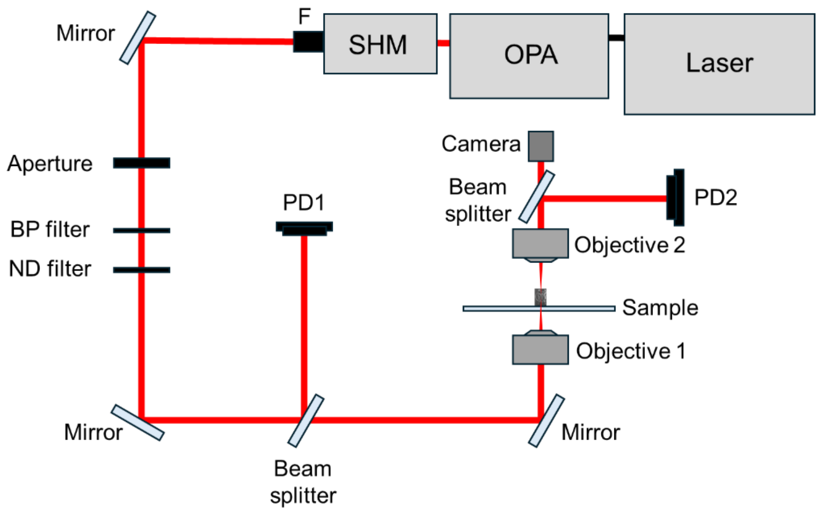

Fig. 13 Schematic representation of transmission and optical performance measurement setup. Laser – Pharos (Light Conversion), λ_{las} = 1030 nm, $t_{pulse} \approx$ 300 fs, OPA – optical parametric amplifier, Orpheus (Light Conversion), pulse tunability from λ_{min} = 650 nm to $\lambda_{\max}$ = 2500 nm, SHM – second harmonics module, Lyra (Light Conversion), $\lambda_{min,2H}$ = 325 nm, F – OPA output beam filter (harmonic separator), Aperture – diaphragm aperture (diameter range: 1 – 20 mm), BP – bandpass filter, ND – natural-density filter, PD1, PD2 – photodiodes, DET100A2 (Thorlabs), spectral range 320-1100 nm. Objective 1 – 20x, NA 0.4, Objective 2 – 10x, NA 0.25.

4. Results

4.1 Optimal MPL fabrication parameters

An array of 50 µm diameter and 10 µm height hemispherical structures, resembling the average diameter of lenses used in BE, was fabricated to evaluate effective printing parameters and identify a stable fabrication window. There were two sets of arrays as depicted in Figures 14, 15. In the first array, laser power and scanning speed were fixed at 1.3 mW and 10 mm/s, respectively, while slicing and hatching distances were varied from 0.05 µm to 0.3 µm, ΔH = 0.05 µm. In the second array, slicing and hatching were fixed at 0.1 µm and 0.1 µm, respectively, while laser power and scanning speed were varied in the range of 0.9–1.8 mW, ΔP = 0.1 mW and 5–14 mm/s, ΔV = 1 mm/s, respectively.

Laser scanning microscope surface analysis demonstrated that slicing distance has a pronounced influence on the profile fidelity of the fabricated hemispheres. In particular, the hemisphere labeled No. 3 in Figure 14 exhibits a clearly defined staircase effect, which is caused by relatively large slicing and hatching distances of 0.3 µm. In contrast, hemispheres No. 1 and No. 2, fabricated with slicing and hatching values of 0.05 µm and 0.1 µm, respectively, yielded smoother surfaces. As slicing and hatching parameters directly determine the number of laser scan lines and, therefore, the total fabrication time, values of S = 0.1 µm and H = 0.1 µm were selected as an optimal compromise between surface quality and fabrication time as larger slicing and hatching values increased printing speed but led to a clearly visible staircase effect, whereas smaller values did not provide a significant improvement in surface quality relative to the increased fabrication time.

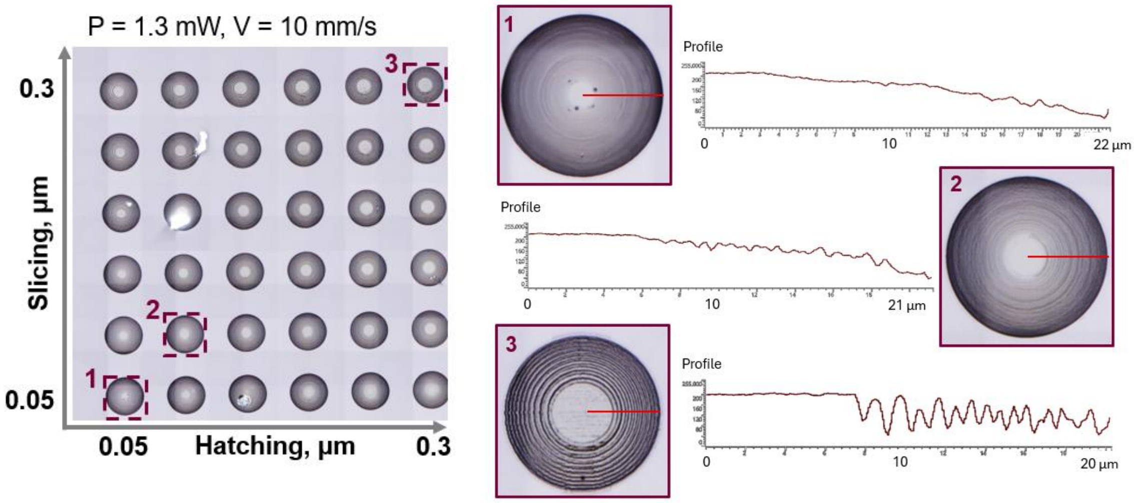

Fig. 14 Images and surface roughness profiles taken with confocal laser scanning microscope. Each structure was printed using different slicing and hatching parameters, as indicated by the numbers. Red line shows profile measurement location.

The influence of laser power (P) and scanning speed (V) on surface morphology was less pronounced than the influence of the slicing parameters – overall surface profile of the microlenses remained relatively similar across the assessed parameter range. Nevertheless, some local defects were observed at increased scanning speeds and laser powers (Fig. 15). These scratch-like features are likely related to less stable voxel formation and non-uniform polymerization at higher scan speeds, where reduced exposure time and less consistent voxel overlap can lead to spatially non-uniform energy deposition.

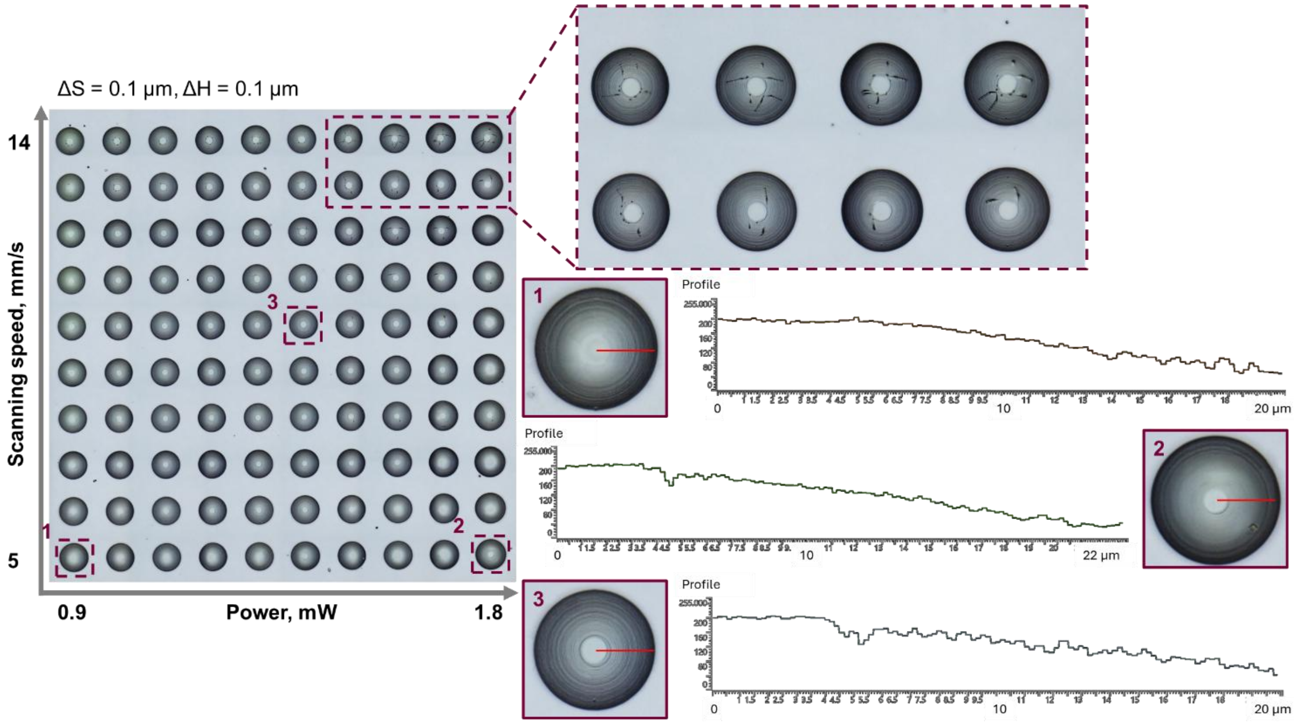

Fig. 15 Images and surface roughness profiles taken with confocal laser scanning microscope. Each structure was printed using different laser power and scanning velocity parameters, as indicated by the numbers. Red line shows profile measurement location.

To further evaluate possible effects of V and P on the structures, height values obtained with confocal laser microscope (described in 3.3) were exported as CSV file and analyzed numerically. For each microlens, the hemispherical form was fitted individually and subtracted from the measured topography, leaving only the residual surface roughness features. One visibly damaged microstructure was treated as an outlier and excluded from the analysis. To minimize artefacts caused by the lens boundary and by form removal errors near the edge, roughness parameters were calculated only from the central 70% area of the microlens. After form removal, S_{dr} parameter was calculated. S_{dr} compares the actual 3D area of the residual surface (with all remaining inhomogeneities after fitted hemisphere removal) with its projected flat area as shown in equation:

$$S_{dr} = \frac{A_{actual} - A_{projected}}{A_{projected}} \times 100\%, \quad (14)$$

where A_{actual} – actual 3D area of the residual surface, $A_{projected}$ – a flat area projected by residual surface.

Therefore, higher S_{dr} values indicate a more pronounced surface roughness with stronger local slopes, hatching and slicing marks or voxel overlap features. In contrast, the commonly used S_a parameter describes only the average absolute height deviation of the residual surface. As a result, two surfaces can have similar S_a values while having different textures. For example, a surface with broad, gradual waviness and a surface with dense fine ridges may show similar average height deviations, but the finely ridged surface will give a higher S_{dr}, because its texture creates more additional surface area. For optical microlenses, this distinction is important because fine surface texture can increase light scattering, whereas broader waviness mainly introduces wavefront distortion or focal aberrations.

S_{dr} shows a clear trend that higher laser power and lower scanning speed result in smoother microlens surfaces compared with conditions using lower power and higher scanning speed. This is visible from the decrease in S_{dr} toward higher *P/V* values (Fig. 16). This tendency could be explained in a way that a higher relative exposure dose can promote formation of bigger voxels and thus greater overlap between adjacent voxels, reducing small surface irregularities and writing-line features. However, this improvement is expected only within a stable processing window. If the local exposure dose becomes too high, excessive voxel growth, over-polymerization, thermal accumulation and material degradation may occur. In the parameter range investigated, the structures retained their hemispherical shape, and no strong evidence of severe overexposure was observed. Localized scratch-like defects were mainly observed at higher scanning speeds, especially when combined with higher laser power. These defects are more likely related to unstable voxel formation, non-uniform polymerization due to excessively high speed rather than to complete burning of the polymer. Therefore, scanning speeds above 12 mm/s were avoided in further fabrication to maintain stable and reproducible microlens formation.

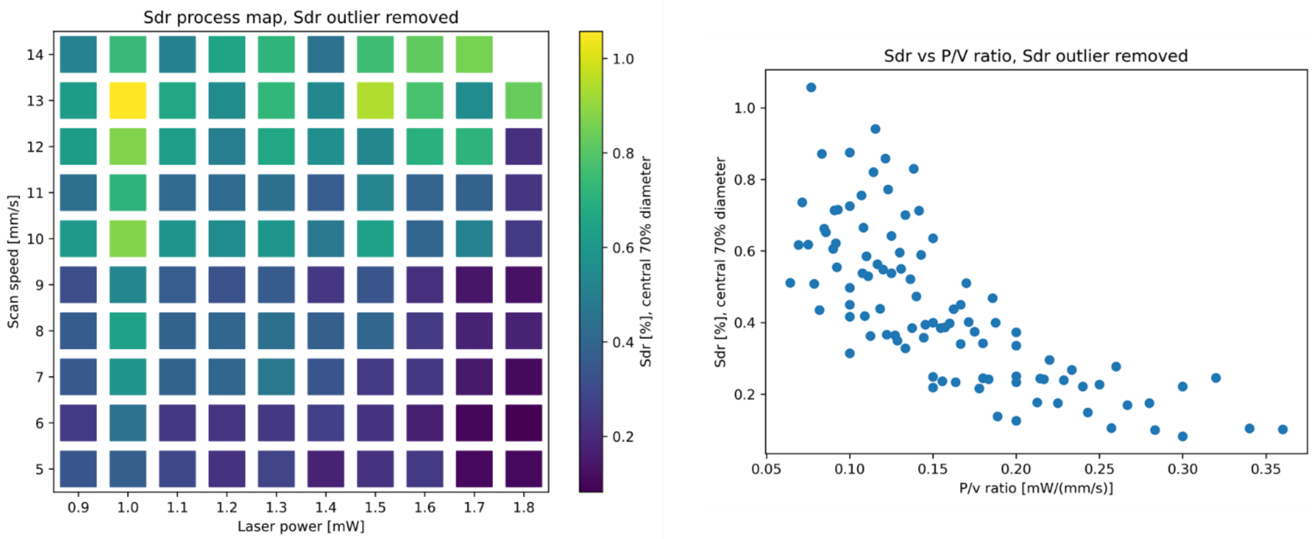

Fig. 16 Surface analysis of the microlens array fabricated with varying laser power and scanning speed. Left plot – S_{dr} value map. Right plot – S_{dr} as a function of the relative P/V ratio, where P is the laser power and V is the scanning speed. Lower S_{dr} values indicate a smoother surface texture.

When fabricating micro-optical components, it is important not only to estimate smallest achievable voxel size, given by wavelength and objective of choice, but also to define the upper fabrication limits of the MPL setup, since they determine the maximum printable diameter of a microlens (without stitching), which is especially important for beam expanders, when the lens diameter directly limits the beam aperture and therefore the maximum achievable beam expansion. Therefore, the lateral working area of the galvo scanner was evaluated by printing squared line structure with 0.1 µm slicing and 0.1 µm hatching. Under the tested conditions, continuous polymerization was achieved over a lateral field of ~200 µm, as shown in Figure 17. Beyond this range, the corners and outer scan paths showed writing defects – discontinuities, detachment, and insufficient polymerization. At larger scan angles optical aberrations, reduced focal quality, field curvature or galvo positioning error likely caused reduction in polymerization reliability. Corners are especially sensitive because they combine scan-direction changes and might be affected by acceleration and deceleration. Therefore, for reliable fabrication, the usable galvo scanner writing field was restricted below 200 µm.

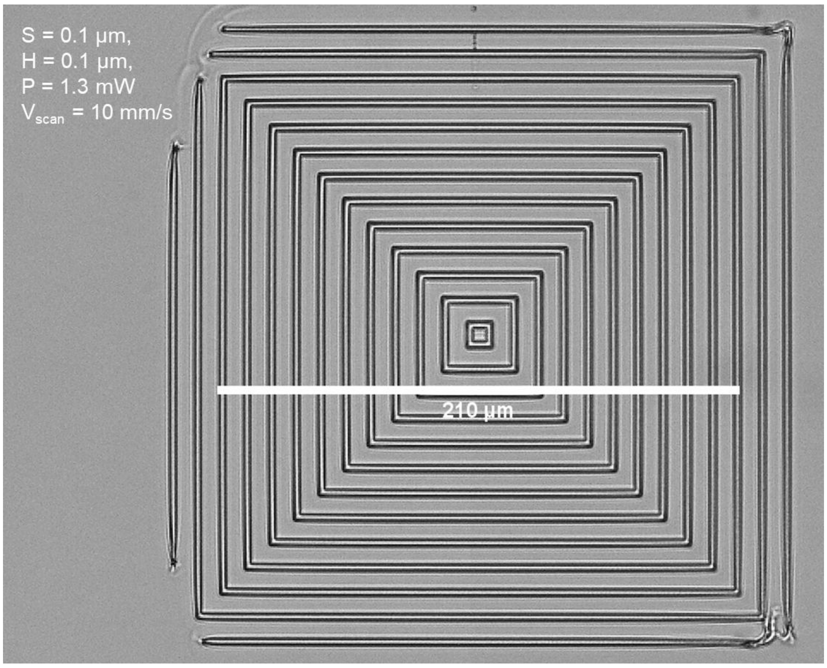

Fig. 17 MPL fabricated structure to evaluate lateral working area. Line thickness – 2 µm, height – 6 µm.

4.2 Structural and morphological analysis of MPL fabricated micro-optical components

To assess how optimal fabrication parameters would translate to actual micro-optic structures with steeper radii of curvature, a test design with 90 µm in maximum diameter and 100 µm in height was printed using 0.2 µm slicing, 0.3 µm hatching distances and 1.2 mW laser power and 10 mm/s scanning speed. SEM imaging only confirmed the results obtained from MPL optimal fabrication parameters. Not only was the slicing (staircase) effect apparent, but also it revealed hatching pattern on the microlens surface as seen in Figure 18. The periodic surface inhomogeneities arising from the discrete layer and scan-line spacing may contribute to increased scattering and loss of optical transmission and could also cause slight intensity modulations as hatching pattern could act as diffraction grating. Despite the presence of surface patterns, the overall contour of the structure remained well defined.

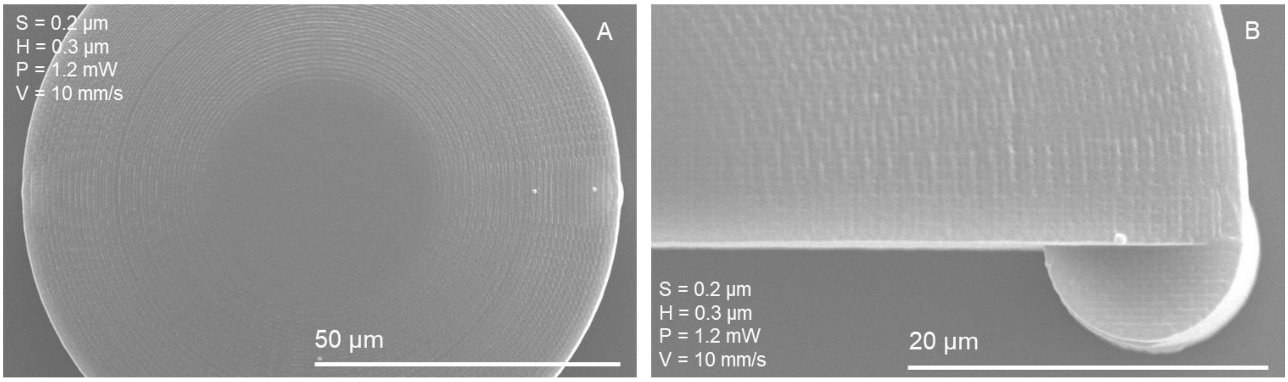

Fig. 18 SEM images of MPL fabricated multi-lens BE test design.

Moreover, initial fabrications revealed a deviation from the intended geometry: the fabricated multi-lens structures exhibited a flattened top surface that was not present in the original design. (Fig. 19) This feature was present across the whole array of samples, indicating that it is a process related effect. One plausible explanation could be exposure onset mismatch, specifically – shutter delay, when scan begins before the shutter is fully open. Consequently, the first part of the written structure receives an insufficient dose and does not polymerize completely.

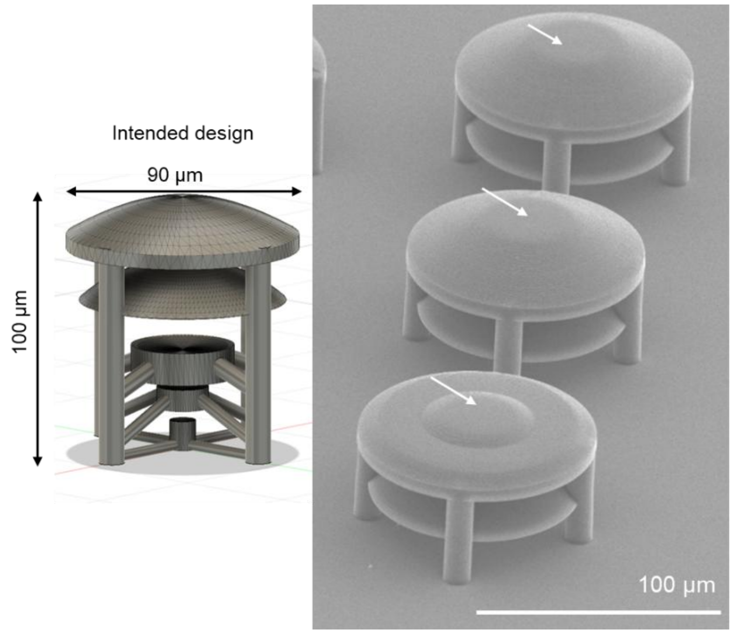

Fig. 19 CAD model of initial design and SEM images of initial multi-lens BE design. White arrows indicate flat top surfaces.

To prevent flat top surfaces, subsequent structures were designed to have protruding supports (Fig. 20) to ensure initiation of polymerization prior to writing the optical elements. As later was observed, this design modification might have solved the issue as later samples did not demonstrate this characteristic.

Furthermore, later fabricated architectures with protruding supports matched the intended form, and no bent, tilted, or cracked structures were detected, indicating mechanical stability when using established printing conditions. Moreover, reducing slicing distance from 0.2 µm to 0.1 µm led to visibly smoother microlens profile, as the staircase effect associated with slicing value was significantly reduced. However, it should be taken into account that structures presented in Figure 20 were fabricated using different laser powers (1.5 mW) than the ones presented in Figure 18 (1.2 mW). Increased laser power increases the voxel size and overlap between adjacent scan lines, therefore also yielding smoother profile.

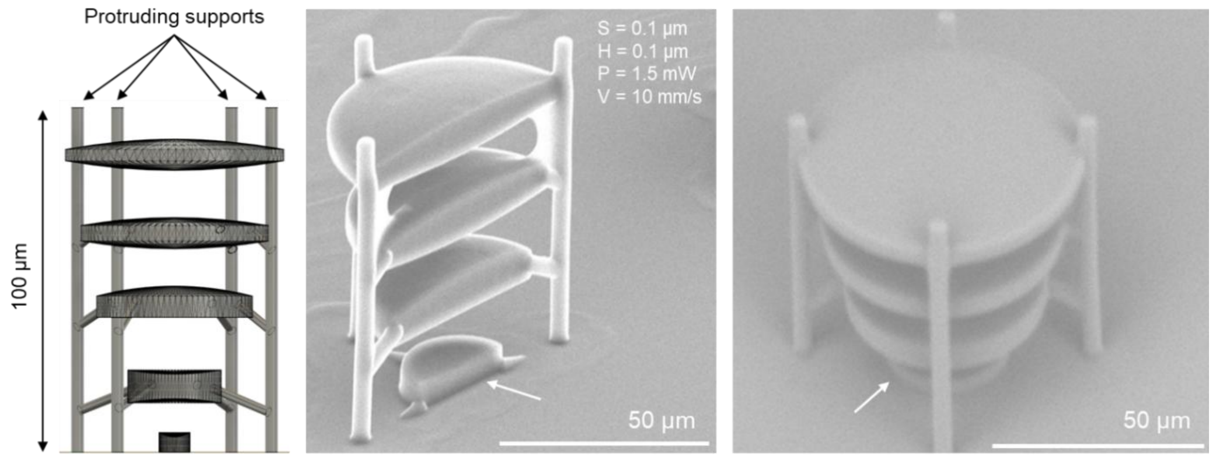

Fig. 20 SEM images of multi-lens BE with protruding supports. White arrows indicate incomplete fabrication arising from sample misplacement on fabrication stage, as a result the lower sections of the structures were truncated, leading to missing lenses near the base.

4.3 Classical type beam expanders

To effectively modulate light with micro-optical devices in confined spaces, e.g. on the tip of a 10 µm optical fiber core, the beam must expand to match the beam shaping device dimensions. This is typically achieved through free-space propagation, however, based on optical simulations, beam divergence can be induced in over 1.6 times shorter distances using beam expanders (BEs). (Fig. 21)

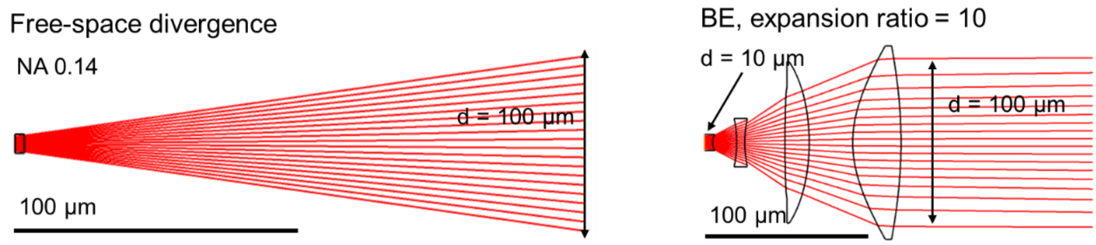

Fig. 21 Comparison of beam expansion in free space and induced by multi-lens BE.

Designs and simulations of BEs were created using Ansys Zemax OpticStudio 2023, R2 optical design software. Simulated collimated light (λ = 633 nm) was coming from infinity and as first optical element in the rays' path was glass substrate (n = 1.52, thickness 170 µm) as structures were printed on borosilicate glass coverslips. Downstream optical elements (lenses) had refractive index set as n = 1.51, corresponding to the refractive-index range of MAPTMS:ZPO molar ratios used in SZ2080^{TM} at 633 nm. [36] As aperture stop first surface of beam expander was set.

Initially classical type Galilean beam expanders having expansion ratios of M = 5, M = 7.5, M = 10, M = 13, M = 15, M = 20 were considered and designed. Focal lengths for each lens were defined based on beam expansion ratio formula (9).

Having determined focal lengths, radius of curvature for each lens was calculated according to lensmaker's equation:

$$\frac{1}{f} = (n-1)\left[\frac{1}{R_1} - \frac{1}{R_2} + \frac{(n-1)t}{nR_1R_2}\right], \quad (15)$$

where f – focal length, n – refractive index, R_1, R_2 – radiuses of curvature of first and second surfaces of the lens respectively, t – thickness. Thickness of first lens was set as 5 μm, for second lens to maintain bigger diameter thus bigger clear aperture the thicknesses varied: 10 μm (M = 5), 15 μm (M = 7.5), 20 μm (M = 10), 25 μm (M = 13, M = 15) and 40 μm for Galilean BEs having expansion ratio M = 20. (*Table 2*) Input lens of all BEs had plano-concave form, second lens of Galilean type BEs had – double convex form. The distance between lens in classical type BEs is defined as the sum of focal lengths of each lens. However, distance between lenses in Zemax is provided as distance between lens' surfaces while focal lengths are set from the principal planes. (Fig. 22) Therefore, the position of principal planes was also considered and calculated according to:

$$h_1 = -\frac{f\,(n_l - 1)\,d}{n_l R_2}, \quad h_2 = -\frac{f\,(n_l - 1)\,d}{n_l R_1} \quad (16)$$

where h_1, h_2 – distance of principal planes from vertices of first and second surfaces respectively, f – focal length, n_l – refractive index of medium (air), d – thickness of lens, R_1, R_2 – radius of curvature of first and second surface respectively.

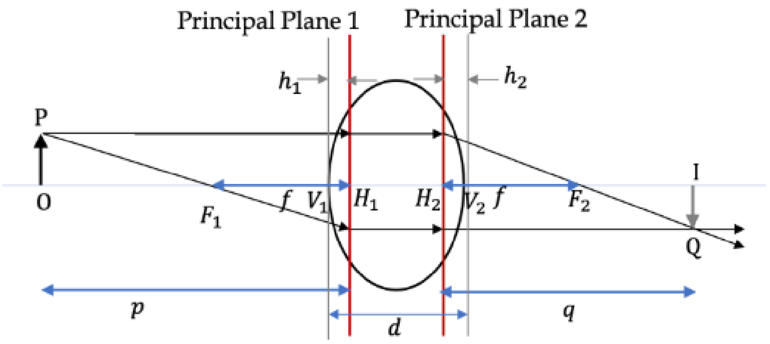

Fig. 22 Cardinal points and principal surfaces of an optical system. *O* - object point, *P* - height of the object above the optical axis, *I* - image point, *Q* - height of the image, H_1 and H_2 - the first and second principal planes of thick lens, h_1 and h_2 - distances from the lens vertices to the corresponding principal planes, F_1 and F_2 - the first and second focal points of the lens, *f* - focal length measured from each principal plane to its corresponding focal point, V_1 and V_2 - the front and back vertices of the lens, *p* - object distance, *q* - image distance. *d* - separation between lens surfaces.

In Zemax software all units were approximated to 1 μm tolerance, since it uses standard ray tracing method and is not well suitable for diffraction limited features. This has led to slight mismatches between calculated design and Zemax simulation therefore, spacing between lens was adjusted manually or by using Optimization tools provided by Zemax software to ensure collimated output. Merit function included ANAR operands to reduce angular spread of output rays, REAR to operands to constrain the ray to the intended beam-envelope diameter and IMAE to mitigate vignetting. Collimation was assessed via direction cosines of spot diagrams at the image plane set 1 mm from last lens surface.

Initial assessment of modelled designs showed first clear limitation dictated by the MPL fabrication setup. To ensure high structural fidelity and minimize voxel size during the MPL process, a high-NA (NA = 1.4, 63x) oil immersion objective was used. However, this objective imposes a maximum working distance of 190 µm. As summarized in *Table 2*, the total required device length (L_{whole}) scales with the expansion ratio of Galilean type BEs. While an expansion ratio of 10 requires a total structure length of 155 µm (within the printable range), scaling the ratio to 13 requires a total length of 230 µm, which exceeds the objective's physical working limit. Therefore, the maximum practically achievable expansion ratio for these classical type Galilean beam expanders was restricted to 10.

Table 2. Design parameters of Galilean BEs. d_1, d_2 – diameter of first and second lens respectively, t_2 – thickness of second lens.

Expansion ratio	d_1, µm	d_2, µm	t_2, µm	L_{whole}, µm
5	10	60	10	97
7.5	10	80	15	105
10	10	110	20	155
13	10	140	25	230
15	10	160	25	277
20	10	210	40	325

Max. working distance of NA 1.4, 63x objective is 190 µm.

The tallest Galilean type beam expander (M = 10, height 155 µm), which is still compatible with the working distance limitation of the 63×, NA 1.4 objective used for MPL fabrication, was printed to evaluate overall structural stability. Four robust support pillars to elevate and maintain the alignment of the final convex lens were designed with a diameter of d = 20 µm. As shown in Figure 23, the complete Galilean BE structure was successfully fabricated, including the 10 µm diameter first lens and the SEM image confirms that the support pillars maintained structure's shape and the main optical elements were printed without obvious misalignment. The faint circular fringes on the top lens are likely tessellation related artefacts arising from insufficient mesh resolution during STL export, therefore for subsequent prints a finer mesh was used.

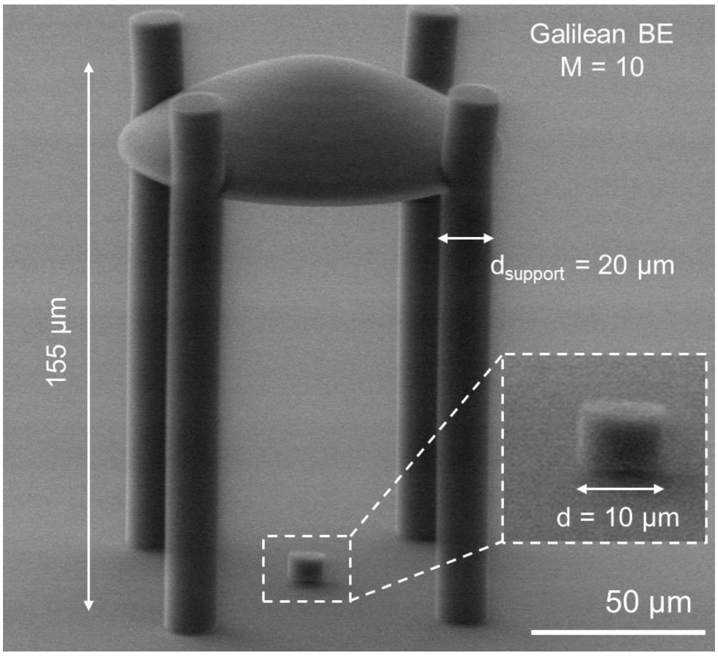

Fig. 23 SEM image of the fabricated Galilean-type beam expander. Printing parameters: S = 0.1 µm, H = 0.1 µm, P = 1.4 mW, V = 10 mm/s.

Sequential ray tracing was used to establish and refine the initial geometrical optics layout, while field propagation was evaluated afterwards with Physical Optics Propagation (POP), which propagates the optical field using scalar diffraction theory. All parameters of simulated Galilean BEs having M = 5, M = 7.5 and M = 10 expansion ratios, are presented in Figure 24 below.

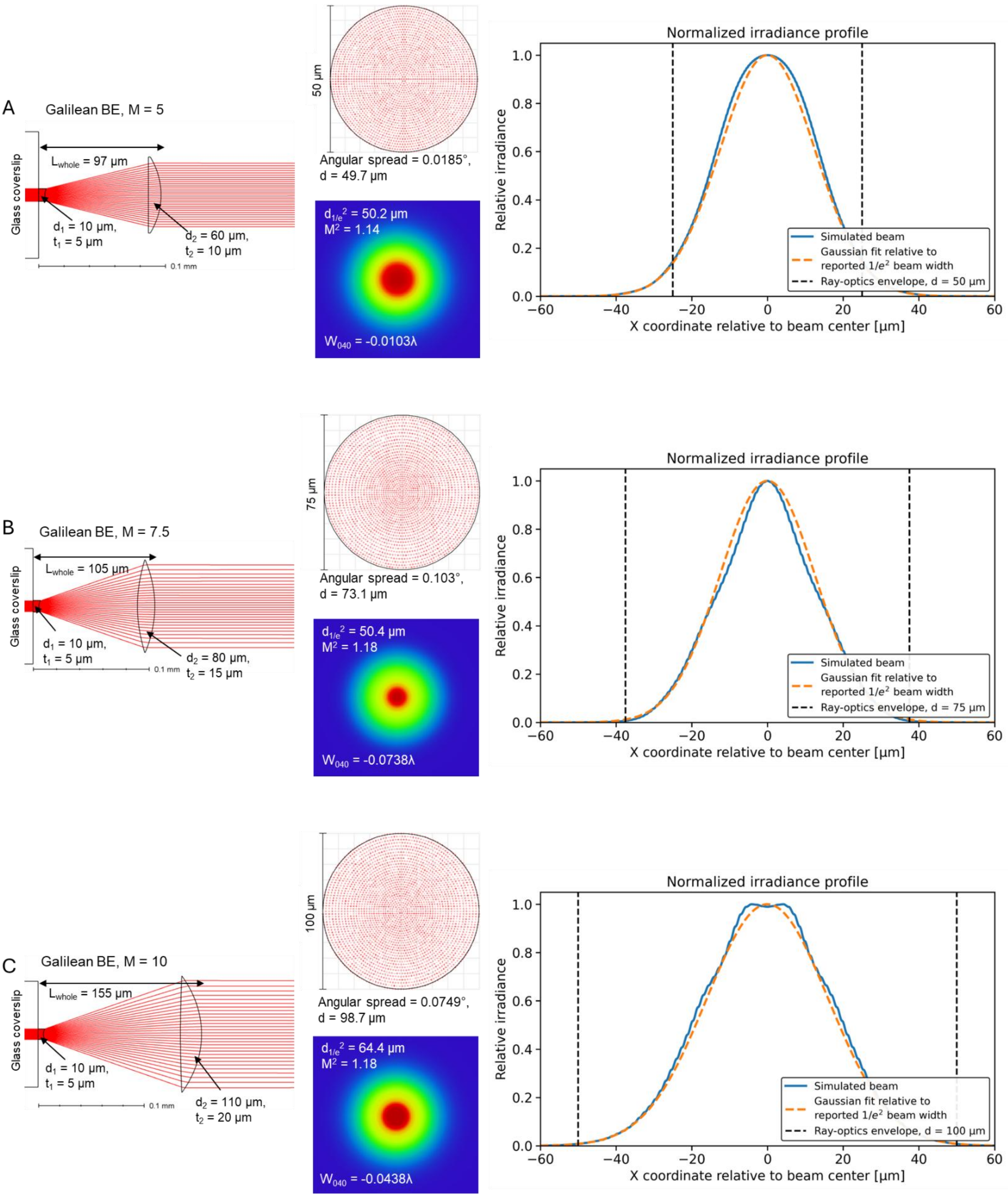

Fig. 24 Design and simulation of Galilean type BEs. Heatmap represents irradiance profile of propagated beam and graphs on right panel represent their intensity cross section.

All designed Galilean type micro-BEs had plano-concave first lens of diameter d_l = 10 µm (which was also an aperture stop for incident beam) and thickness t_l = 5 µm, while second lens initially set as double-convex lens after optimization either remained their shape (in M = 7.5 case) or became plano-convex. Ray-tracing results show that all three designs reached the intended geometrical expansion. The output ray-envelope diameters at the evaluation plane were 49.7 µm, 73.5 µm and 98.7 µm for M = 5, M = 7.5, M = 10 designs, respectively. These values should be interpreted as geometrical ray-envelope diameters, rather than Gaussian $1/e^2$ beam diameters. The geometrical collimation performance was evaluated using the angular spread of the ray bundle. Stronger deviation from intended diameter had M = 7.5 BE, but this could be attributed to optimization constrains, since optimization operand took radius of intended diameter, setting precisely r = 37.5 µm for M = 7.5, was impossible due to unit approximation to 1 µm. Moreover, M = 7.5 BE showed vignetting, resulting in ~97% of transmitted rays. From ray-optics standpoint, the M = 5 design demonstrates best collimation performance, with the smallest angular spread (~0.019°) as calculated by directional cosines of marginal rays relative to the optical axis. In contrast, the M = 7.5 and M = 10 designs exhibited larger angular spreads ~0.1° and ~0.075°, respectively. These values represent purely geometric collimation errors and should not be interpreted as the full physical beam divergence, because diffraction-limited beam divergence half angle calculated by $\Theta = \frac{\lambda}{\pi\omega_0}$, where λ – wavelength, ω_0 – Gaussian diffraction limited beam radius at $1/e^2$, would dominate and lead to several times larger divergence than geometrical angular spread.

To account for these physical effects, scalar diffraction simulations were conducted using Zemax Physical Optics Propagation (POP), inputting a perfect Gaussian beam of ω_0 = 3 µm at the lens surface. The resulting irradiance cross-sections and heatmap profiles indicate that all three designs preserve a near-Gaussian beam profile (M^2 = 1.14 for M = 5 and M^2 = 1.18 for both M = 7.5 and M = 10). However, for integrated light-modulating applications, preservation of the output phase is also critical, since the downstream device acts on the complex optical field rather than on the irradiance profile alone. Ray-based Seidel analysis indicated that the dominant residual aberration was primary spherical aberration, with W_{040} = -0.0103λ, -0.0738λ, and -0.0438λ, for M = 5, M = 7.5 and M = 10, respectively. These values indicate weak residual spherical aberration. However, Seidel coefficients describe the geometrical lens aberration and do not fully represent the propagated Gaussian field. For this reason, the POP phase profiles were used as the more relevant scalar-field assessment of output wavefront quality. Scalar optics revealed that the total peak-to-valley phase distortions at their respective measurement planes were 0.48λ for M = 5 BE, 0.35λ for M = 7.5, and 0.29λ for M = 10. Given that the Rayleigh peak-to-valley reference for wavefront quality is <0.25λ [28], the output wavefronts have residual phase curvature relative to an ideal plane wavefront. Increasing the expansion ratio of BEs improves the output wavefront flatness, which could be explained by the larger output beam diameter. A larger Gaussian beam has a longer Rayleigh range, and it spreads less over the same distance, as a result, the wavefront curvature is less pronounced, and the output phase is flatter. This suggests that the classical Galilean BEs have limited freedom to simultaneously control beam expansion, ray-envelope diameter, angular spread, and output wavefront flatness. Therefore, the transition to a multi-lens BE design with additional optical surfaces might provide more degrees of freedom to control optical power and improve the output beam quality.

4.4 Compact multi-lens beam expanders

In a Galilean beam expander, the first optical element is a negative lens that intentionally diverges the incident beam before it is re-collimated by the subsequent positive lens. Thus, rays entering the system at larger radial positions experience stronger refraction and propagate at higher angles after the first element. Therefore, not all rays are fully re-collimated by the second lens as it is indicated by the marginal rays in Figure 25. This could cause vignetting and partial loss of the beam.

To address that problem, second (converging) lens could be larger in diameter, but MPL has lateral limitations imposed by objectives field of view and galvano-scanner system, if not considering stitching which would present its own problems. Thus, another approach to tackle the issue is to design multi-lens beam expanders for distributing optical power across multiple lenses. (Fig. 25)

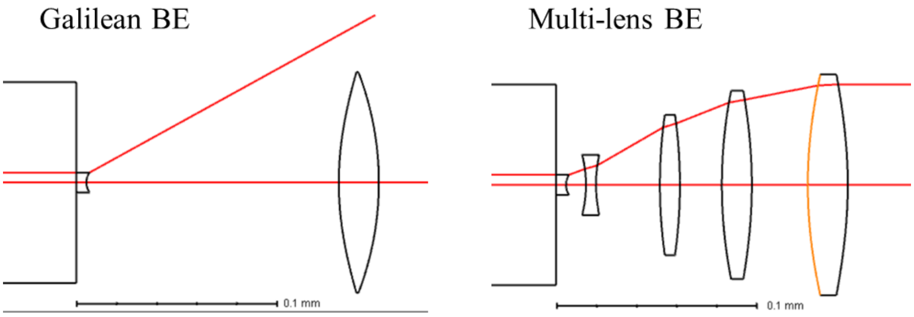

Fig. 25 Schematic representation of Galilean and multi-lens BE (M = 10) Zemax simulation with only marginal and chief rays.

Taking classical Galilean type BEs as reference, multiple lenses were inserted and simulated. The main immediate difference was the reduced total system length required to achieve the same expansion ratio. For M = 5, the multi-lens design reduced the total length from 97 µm to 66 µm which accounts for ~30% and for M = 10, the length decreased from 155 µm to 122 µm, ~21%. Moreover, multi-lens approach enabled higher expansion ratios that were not achievable with the classical Galilean design, such as M = 15, with total length of 159 µm and even M = 20 approaching working distance limit of the objective with total length of 187 µm. (*Table 3*)

Table 3 Design parameters of multi-lens BEs. L_{whole} – total optical system length, t_{print} – printing time with MPL system. Bolded line shows working distance limit of the objective used in this work.

Expansion ratio	Galilean L_{whole}, µm	Multi-lens L_{whole}, µm	Galilean t_{print}	Multi-lens t_{print}
5	97	66	20 min	15 min
10	155	122	1 h 51 min	1 h 40 min
15	277	159	-	3 h 45 min
20	325	187	-	-

Ray-optical simulations (Fig. 24, 26) show that the multi-lens design gives better control of the geometrical output diameter compared to Galilean designs. The ray-envelope diameters here were 50.0 µm, 99.8 µm and 150.0 µm for M = 5, M = 10, and M = 15, respectively. The angular spread, however, does not improve uniformly with the multi-lens approach. For M = 5, the Galilean BE has lower angular spread (0.0185°) than the multi-lens BE (0.0570°). For M = 10 the Galilean BE is also lower (0.0749°) than multi-lens BE (0.377°). However, the multi-lens M = 15 design gives a very low angular spread of 0.0045° showing excellent ray-optical collimation. As before, these values should be interpreted as geometrical collimation errors rather than full physical beam divergence, because diffraction of the finite Gaussian beam still contributes strongly at this scale.

The POP irradiance results show that the M = 5 multi-lens BE follows the Gaussian fit closely, and the beam quality factor remains low at $M^2 = 1.17$, which is comparable to the Galilean M = 5 with $M^2 = 1.14$. This suggests that at low expansion ratio, the multi-lens approach can reduce length without strongly degrading the beam profile. The M = 10 and M = 15 designs show more noticeable deviations from an ideal Gaussian profile, which could be seen as flattened tops and ripples in irradiance profile. This is also reflected in the increase of M^2 to 1.23 for M = 10 and 1.40 for M = 15. Therefore, while the multi-lens approach improves geometrical scalability and allows larger expansion ratios, it introduces stronger intensity profile distortion. The simulations indicate that the multi-lens systems give more control over expansion and geometrical collimation, but the increased number of refractive surfaces can also introduce interference, diffraction, or residual phase/amplitude modulation.

The POP phase profiles provide the clearest distinction between the three multi-lens BEs. Peak-to-valley phase variation was approximately 0.45λ, 0.31λ, and 0.13λ for M = 5, M = 10, and M = 15, respectively. This shows that the M = 15 multi-lens design gives the flattest output phase among the three designs and is the only one below the classical λ/4 peak-to-valley reference and is lower than the best Galilean value previously obtained. Although the M = 5 design preserves the cleanest Gaussian irradiance profile, its output phase has the largest peak-to-valley variation. The M = 15 design shows the opposite behavior - the irradiance profile is less Gaussian and M^2 is higher, but the phase profile is significantly flatter. Therefore, increasing the expansion ratio in the multi-lens architecture improves output phase flatness and geometrical collimation, but at the cost of increased amplitude-profile distortion.

Overall, the multi-lens architecture provides improvement over the classical Galilean design in terms of compactness, achievable expansion ratio, and output phase control. However, for M = 10 and M = 15 this improvement is accompanied by degradation of the irradiance profile and an increase of M^2. Therefore, the multi-lens approach is advantageous for integrated light-modulating devices where output phase uniformity and compactness are prioritized, but the main disadvantage is stronger deviation from an ideal Gaussian profile, especially for M = 10 and M = 15. In addition, comparison of ray envelope with actual $1/e^2$ beam diameter in both Galilean and multi-lens BE designs indicates, that ray-tracing based simulations should be used only as a preliminary design as is useful for defining the geometrical layout, expansion ratio, and marginal-ray envelope, but it does not fully describe the physical Gaussian beam propagation in micro-optics. Therefore, final evaluation must include at least scalar optics propagation, when output beam diameter, irradiance distribution, phase flatness, and wavefront quality are important.

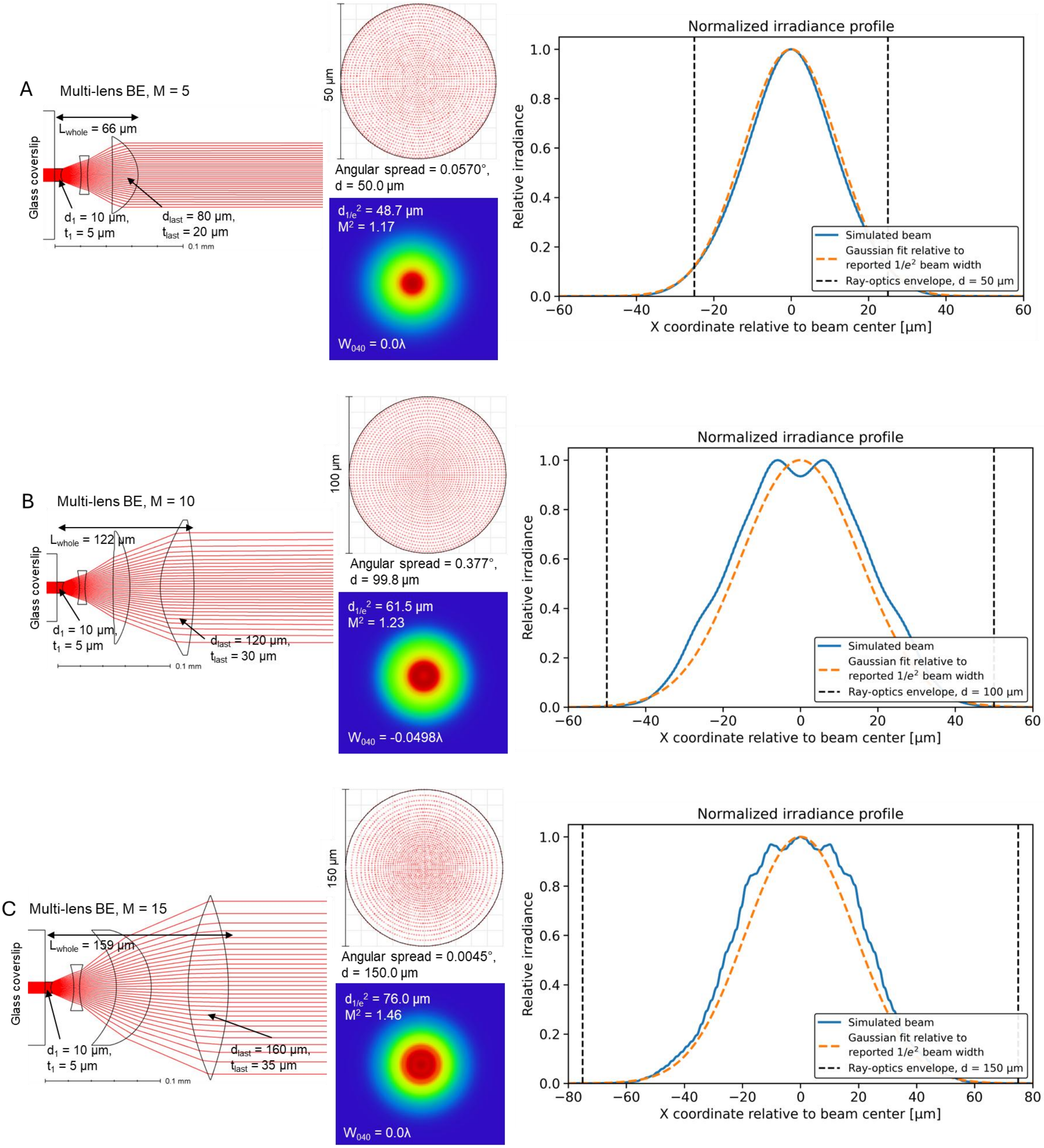

Fig. 26 Design and simulation of multi-lens BEs. Heatmap represents irradiance profile of propagated beam and graphs on right panel represent their intensity cross section.

It is also worth noting that each surface of micro-optics would induce loss of transmission, mainly due to Fresnel reflections. Since SZ2080^{TM} is transparent in the range of ~550 – 800 nm (Fig. 9), light attenuation due to absorption at the wavelength used for design (633 nm) is considered negligible. The reflection for the light incident on the different refractive index material surface at 0° angle can be described by the Fresnel formula:

$$R = \frac{(n_1 - n_2)^2}{(n_1 + n_2)^2} \quad (17)$$

where n_1 – refractive index of one optical media (air) and n_2 - refractive index of another optical media (in this case polymer). It accounts for $R \approx 4\%$ per surface. When multiple lenses are present in an optical system the total light transmission can be calculated using formula:

$$T = T1 * T2 * \ldots * Tj, \quad (18)$$

where Tj – transmission at each optical interface. In practice, light attenuation of the whole optical system can be up to 27% for 3 - element structures. [15] Therefore evaluating transmission of fabricated BEs is necessary for further optimizations. To assess the transmission, platform structures having flat surfaces and resembling average lens thickness of BEs were fabricated. Each structure consisted of 2, 3, 4 platforms. The platforms were 120 μm in diameter and 15 μm thick with 15 μm air gaps between adjacent layers. The resulting total structure heights, measured from the substrate surface to the top surface of the final platform, were 60 μm, 90 μm, and 120 μm for 2, 3 and 4 platform structures, respectively. Based on Fresnel reflection losses, the expected transmission values were 84.5%, 77.6%, and 71.3%. Transmission measurements were performed at λ = 633 nm using the setup described in Section 3.4, and the acquired values are summarized in *Table 4*.

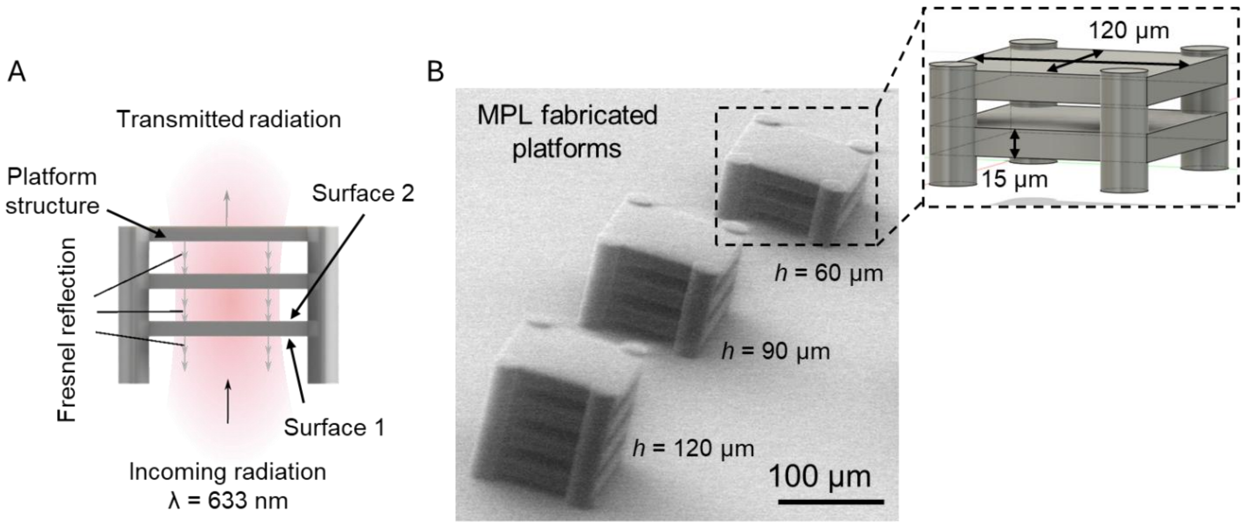

Fig. 27 A – Schematic representation of Fresnel reflection losses at multiple polymer-air interfaces, B – MPL fabricated microstructures, h – total height of a platform from substrate to the last surface. Printing parameters: ΔS = 0.2 μm, ΔH = 0.2 μm, V_{scan} = 10 mm/s, P = 1.6 mW.

Table 4. Theoretical and experimentally measured transmission values of MPL printed platform structures at λ = 633 nm.

No. of surfaces	Estimated transmission	Measured transmission
4	84.5%	~83%
6	77.6%	~75%
8	71.3%	~69%

Transmission values obtained experimentally were slightly lower than theoretically estimated ones and resulted in approximately 83%, 75%, and 69% for structures with 2, 3, and 4 platforms, respectively. The trend of decreasing transmission as the number of interfaces increases suggests that Fresnel reflection was the dominant factor governing transmission loss. Additional reduction in measured transmission, observed as the difference between theoretical and experimental values, is likely caused by fabrication related surface roughness or slicing artefacts, which cause additional light scattering.

Furthermore, similar platform structures having 3 platforms and different individual platform thicknesses were fabricated to assess whether polymer thickness affect transmission at λ = 633 nm. The platform thicknesses were 10 µm, 15 µm, and 20 µm and measured transmission values were ~76%, ~75%, and ~73%, respectively. (Fig. 28) Since the transmission changed only slightly over this thickness range, the results only support that absorption in SZ2080^{TM} at 633 nm is negligible compared with interface related Fresnel losses. The small variations in the measured transmission values may arise from measurement fluctuations and fabrication related scattering induced by slicing artefacts or minor internal inhomogeneities. For thicker platforms, the increased polymer volume (thus longer light propagation path through the polymer) may enhance the influence of these effects, resulting in a slight reduction in measured transmission.

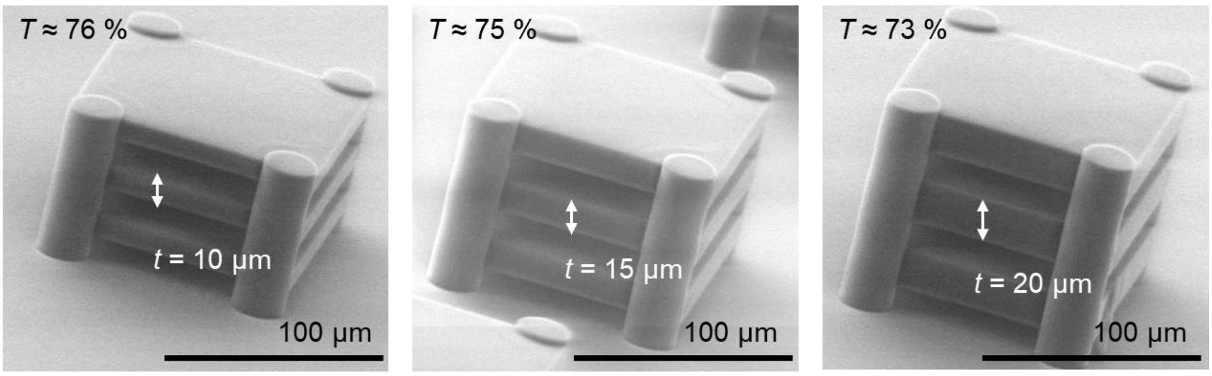

Fig. 28 MPL fabricated platform structures having different thicknesses (*t*) of platforms. Printing parameters: ΔS = 0.2 µm, ΔH = 0.2 µm, V_{scan} = 10 mm/s, P = 1.6 mW.

Overall, the results show that MPL-fabricated multilayer structures maintain high transmission at 633 nm. Even for the structure containing 8 surfaces, the measured transmission remained close to 70%. This demonstrated promising results that the fabrication process and resin of choice is suitable for producing and testing micro-optics with acceptable optical throughput. Further optical improvements could be achieved by reducing surface roughness or applying anti-reflection strategies, more discussed in 5.5.

Moving further to the optical performance of the MPL fabricated BEs, an initial assessment was performed to roughly assess whether the multi-lens M = 10 BE had effect on the incoming beam. The setup described in Section 3.4 and schematically shown in Figure 29 was used, where the incoming 633 nm beam was focused onto the coverslip-BE interface. The beam was propagating over a distance of z = 6 cm, both with the M = 10 multi-lens BE and without any structure present. The resulting beam diameter at the measurement plane was estimated visually from the visible intensity distribution.

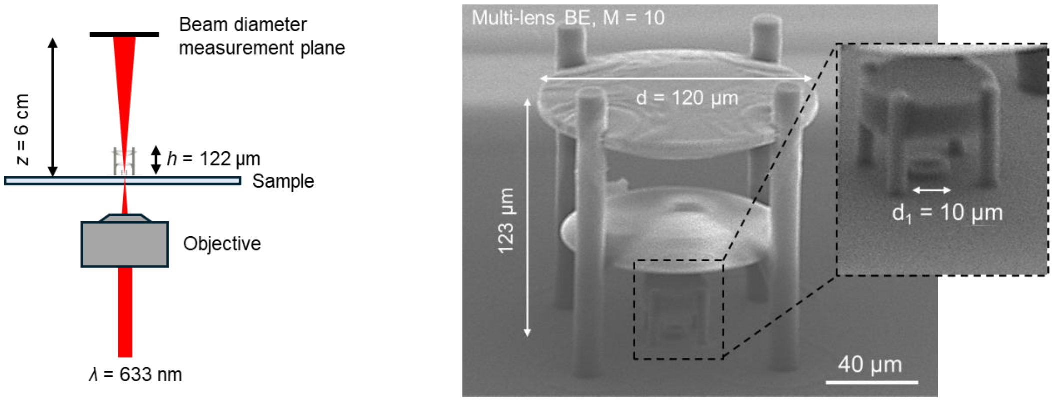

Fig. 29 Right panel - schematical representation of the initial optical performance assessment of fabricated BE. The beam diameter was estimated after 6 cm of free-space propagation with and without the fabricated BE. Left panel – SEM image of MPL fabricated BE, M = 10.

Experiments showed reduced beam divergence at a propagation distance of 6 cm. Freely propagating beam expanded to a diameter of approximately 14 mm, while the beam leaving the M = 10 multi-lens BE measured roughly 8 mm in diameter, representing a ~1.8 times reduction in beam expansion at the measurement plane. The remaining divergence indicates that the experimentally observed output beam differed from the idealized Zemax simulations and several factors may contribute to this difference, including optomechanical misalignment within the measurement setup and fabrication imperfections such as surface roughness, deviations from intended design, which induce additional diffraction and scattering. Moreover, condition mismatch existed between the simulated design and the empirical testing environment. BEs were optimized for a perfectly collimated input beam with flat wavefront and in the experimental setup the input beam was focused using a 0.4 NA objective, injecting a highly divergent cone of light with significant angular spread into the lens system. Because BE was not optimized with sufficient optical power to collimate such extreme input divergence, it only scaled the divergence angle down rather than eliminating it entirely. Nevertheless, the observed 1.8-fold reduction in beam diameter under these non-ideal input conditions provides empirical evidence that fabricated multi-lens BE influences the output beam in the expected manner by reducing its divergence compared to free space propagation, even though ideal collimation was not achieved.

An additional assessment of the optical performance of the MPL fabricated M = 10 beam expander was performed by capturing the output beam at several axial positions. The input beam was focused onto the sample, and 6 beam profile images were taken with a 100 µm axial step, starting from the coverslip/BE interface. The same measurement was carried out in the BE region and in a reference region containing only coverslip. After background subtraction, the beam profiles were analyzed by extracting the averaged central $1/e^2$ diameter from multiple neighboring horizontal and vertical cross-sections as shown in Figure 30, where green lines represent averaged envelopes of normalized $1/e^2$ intensity in x and y directions and cyan and purple shadows represent cross sections used for averaging.

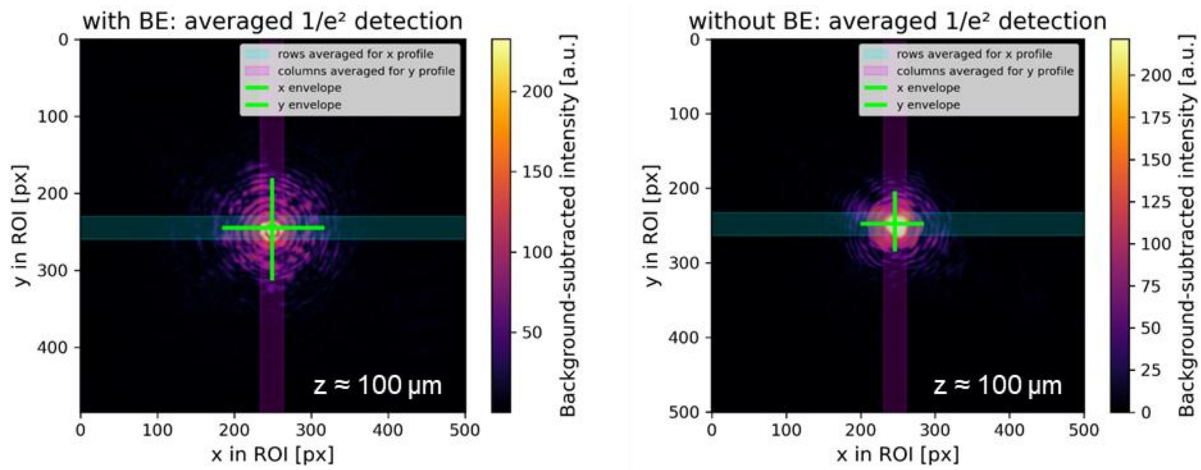

Fig. 30 Background-subtracted beam intensity profiles of freely propagating beam and beam passing through BE. Green lines represent averaged envelopes of normalized $1/e^2$ intensity in x and y directions and cyan and purple shadows represent cross sections used for averaging.

Results show, that the central $1/e^2$ diameter was initially larger for the beam propagating through the BE region than for the reference beam propagating in free space. (Fig. 31) Since the BE height is approximately 122 µm, these initial measurement planes at ~100 µm likely correspond to propagation inside the fabricated microlens. This suggests that the BE broadens the beam already inside the structure. At larger propagation distances, the reference beam expands more strongly, while the beam after the BE remains smaller. This behaviour supports the previous measurement, where reduction of beam diameter after propagation through BE was observed. These results imply that the MPL-fabricated BE modifies the beam in the intended direction by broadening the beam within the structure and reducing its subsequent divergence, although the measured beam profiles remain non-ideal.

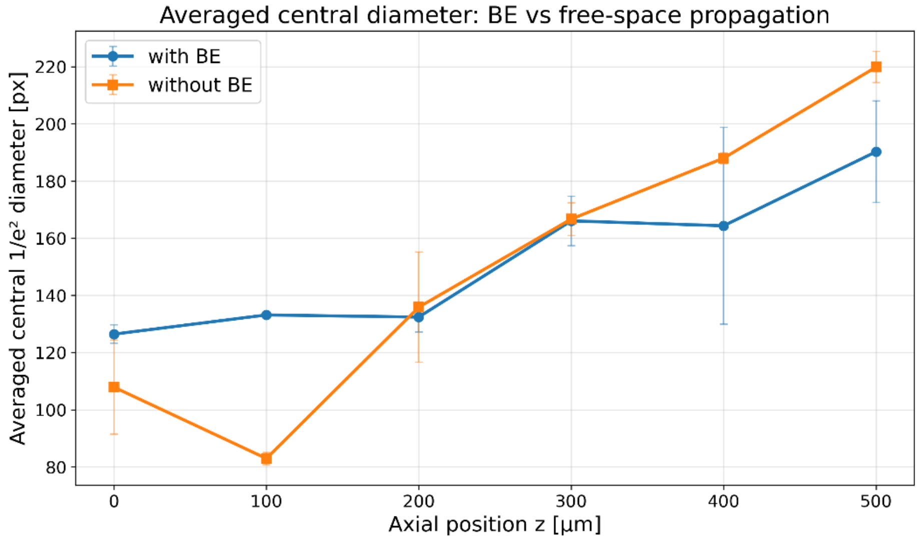

Fig. 31 Comparison of the averaged $1/e^2$ beam diameter as a function of axial position for beam propagation with BE and in the region without BE. Error bars indicate the spread between the horizontal and vertical $1/e^2$ diameter measurements.

Moreover, as mentioned in Section 2.4, scalar optical simulations become less complete for micro-optical components operating at relatively high numerical apertures with large ray angles. Examples given in Figure 32 show single lenses which are present in multi-lens BE design. The first diverging lens, with a diameter of 10 µm, had reported working f-number = 1.43, corresponding to an estimated numerical aperture of NA = $\frac{1}{2\,f\#}$ ≈ 0.35. The final focusing lens with a diameter of 160 µm, had working f-number = 1.23, corresponding to NA ≈ 0.41. These values indicate that the microlenses operate in a moderate-to-high NA regime, where polarization dependent effects may become relevant. Therefore, although scalar simulations provide a more realistic description than ray tracing by including diffraction and phase propagation, they should still be treated as an approximation. This also may explain deviations between the simulated beam expander performance and the experimental optical performance measurements.

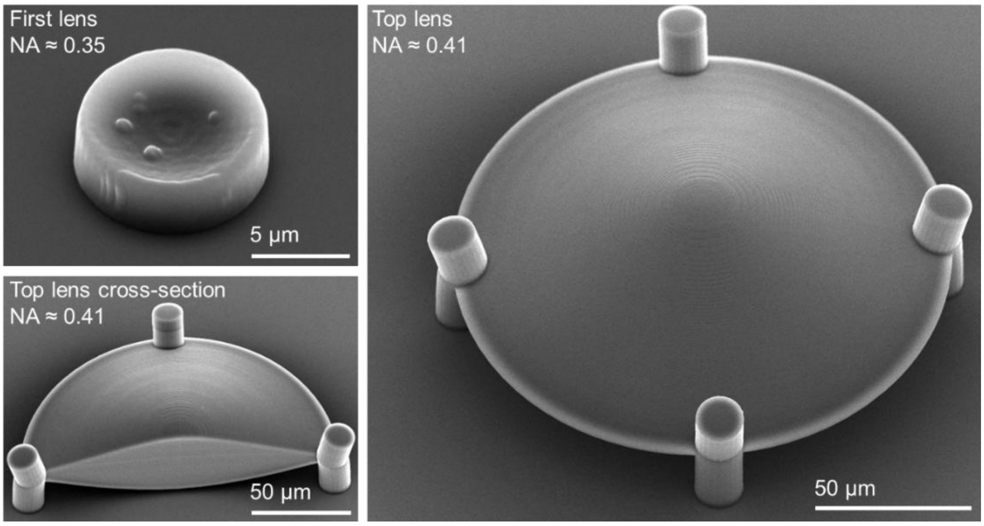

Fig. 32 SEM images of single lens from multi-lens BE, M = 15 design.

4.5 Light modulating devices – Spiral phase plates

Spiral phase plates were fabricated to further explore the capabilities of precise manufacturing enabled by MPL using high-NA objective. As discussed in Section 2.2 SPPs shape wavefront by introducing an azimuthally varying phase delay around the optical axis. The required spiral height depends on the wavelength (λ), refractive index contrast (Δn), and the desired topological charge (l), as equations (6)-(8) suggest. For 633 nm and Δn = 0.51 the designed heights were $h_{2\pi}$ = 1.24 µm, $h_{4\pi}$ = 2.48 µm, $h_{6\pi}$ = 3.72 µm for topological charges l = 1, l = 2, and l = 3, respectively. Here SPPs had diameter of 150 µm and a 5 µm base layer was included to ensure that the spiral profile of an SPP was fabricated fully inside the photoresist. (Fig. 33, A)

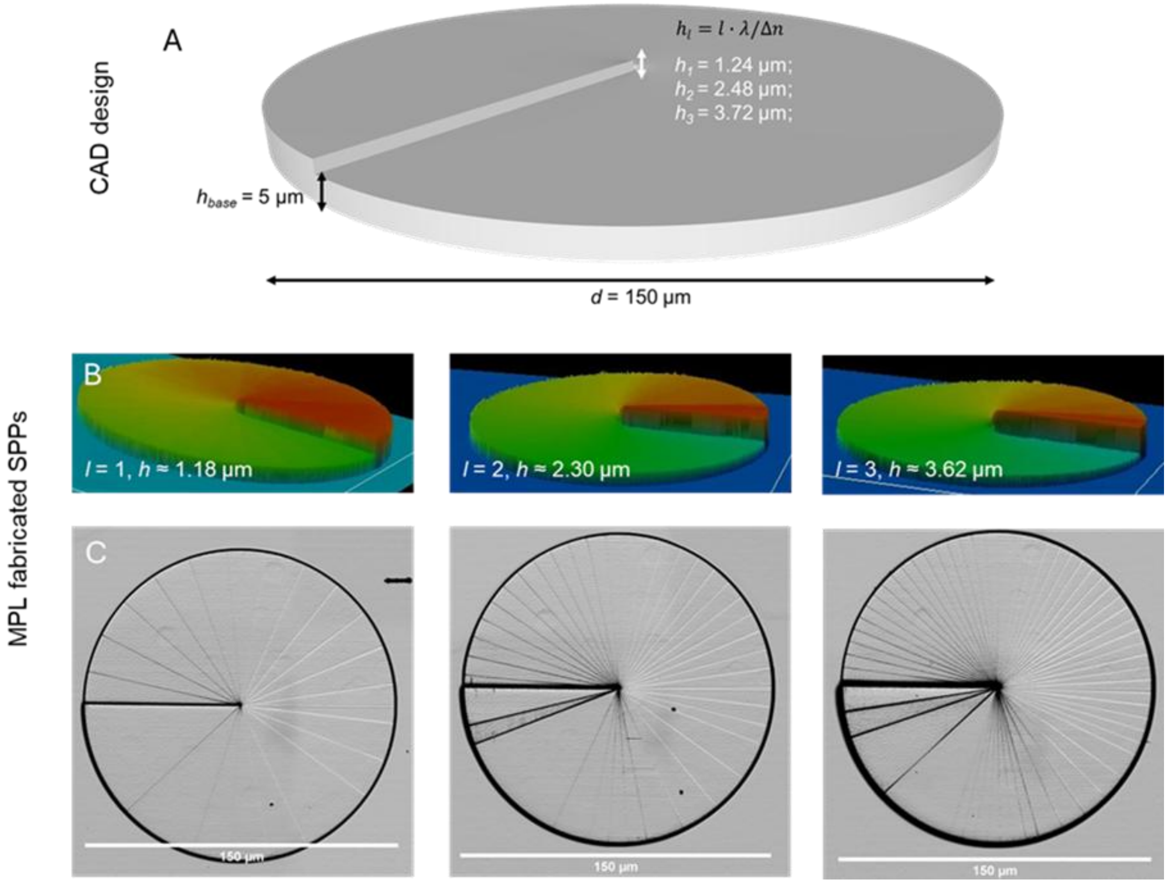

Fig. 33 Design and fabrication results of MPL-printed spiral phase plates. A – CAD model of SPP, B – height maps of MPL printed SPPs, C – confocal microscope images with enhanced contrast, showing the fabricated SPPs top surface. Printing parameters: ΔS = 0.05 µm, ΔH = 0.2 µm, V_{scan} = 10 mm/s, P = 1.3 mW.

The fabricated structures reproduced the intended spiral geometry for all three topological charges. The height maps show a continuous azimuthal ramp and a steep spiral discontinuity, as expected for SPPs. However, fabricated SPPs experienced height deviation from initial design values resulting in $h_{2\pi} \approx 1.18$ µm, $h_{4\pi} \approx 2.30$ µm, $h_{6\pi} \approx 3.62$ µm after printing and developing. These values correspond to deviations of approximately 0.06 µm, 0.18 µm, and 0.10 µm, respectively. (Fig. 33, B) This might have been caused by shutter delay during fabrication, polymer shrinkage, or discrete slicing step (ΔS) of 0.05 µm. So-called staircase patterns (radial lines) are also visible in the confocal microscope images. (Fig. 33, C) These are expected MPL fabrication artefacts because the 3D shape is produced by discrete scan paths and slicing steps. The visible radial features become more denser and narrower as the topological charge increases, because the overall phase ramp is steeper, therefore more slicing steps are needed to complete the 3D structure.

Although the overall SPP geometry was successfully reproduced, the height deviations might have influence on the optical performance of SPPs because the phase delay introduced by an SPP is proportional to the structure height and deviations are expected to reduce the completeness of the intended wavefront transformation. In practice, this may lead to a phase shift below the ideal 2π, 4π, 6π values and together with staircase effect may reduce the purity of the generated optical vortex.

To test the optical performance of fabricated SPPs the setup described in Section 3.4 was used. First simulation was conducted and results were compared with actual optical performance of SPPs. The simulation models the input as a Gaussian beam at the SPP plane with a Gaussian intensity profile and a curved wavefront. Based on a 0.40 NA focusing objective used in the experimental setup, the model estimates a diffraction-limited waist of about 0.97 μm, placing the SPP plane approximately 122 μm away from the waist. This gives a wavefront curvature radius and ~50 μm input beam diameter corresponding to approximate input beam diameter in physical setting. The curvature phase accounts for the beam being defocused at the SPP plane rather than perfectly collimated, making the simulation more representative of the experimental geometry. The SPP imposes an azimuthally varying phase profile corresponding to the selected topological charge. In the simulation, this was implemented by multiplying the Gaussian input field by the complex phase factor $e^{(il\phi)}$, where i – imaginary unit, l – topological charge and ϕ - angle around the optical axis. The transmitted field is then propagated over 100 μm using the angular-spectrum method (explained in section 2.4). To approximate the experimental imaging conditions, the propagated field is filtered by the numerical aperture of the collection objective (0.25 NA). This represents the finite angular acceptance of the collection objective – light propagating at angles larger than the objective can collect is removed. It removes high spatial frequency components, which correspond to light propagating at larger angles relative to the optical axis. Therefore, after filtering, abrupt transitions such as the ring edges and the boundary of the central minimum become more gradual. After propagation through the SPPs, the simulated beams exhibit a characteristic central intensity null whose diameter increases with the topological charge. Weak diffraction fringes are also observed and can be attributed to mode mismatch – the SPP imposes a helical phase on the Gaussian input beam without enforcing the radial amplitude profile of a pure Laguerre–Gaussian mode, leading to additional radial components that interfere during propagation.

Simulation results were compared to actual optical performance of MPL fabricated SPPs. The mvBlueFOX 223C camera used for image capture is specified as a 1360 × 1024, 1/2″ CCD camera. The reported pixel pitch for this specific sensor is 4.65 μm × 4.65 μm. [39], [40] With the 10x imaging objective, the object plane scale is ~0.465 μm/pixel. Based on this calibration, the input beam diameter for optical assessment of SPPs was ~50 μm. After passing through the fabricated SPPs, beams showed vortex-like intensity distributions, including a characteristic central intensity minimum whose size increased with the topological charge, suggesting that the fabricated SPPs induced helical phase modulation in the propagating beam. Compared with the simulated profiles, the experimental intensity distributions exhibited stronger asymmetry and distortion, likely arising from non-ideal fabrication, the stepped SPP profile shown in Figure 33, C, alignment errors in the measurement system, and input-beam imperfections.

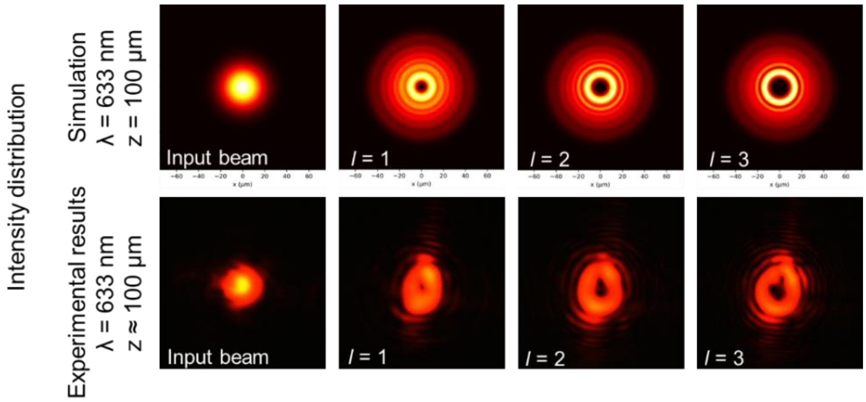

Fig. 34 Simulated (top) and experimentally achieved (bottom) vortex-like intensity distribution.

To further explore the printing capabilities, arrays of phase-modulating microstructures were fabricated using two different slicing/scanning speed parameter sets as shown in Figure 35. The input beam is shown on the left for reference. Structures with topological charges $l = 1$, $l = 2$, and $l = 3$ were printed and tested. The resulting intensity profiles show the expected redistribution of the input beam into ring-like patterns with a central intensity minimum, indicating that the printed structures modify the optical phase of the incident beam. The obtained optical performance images show that the optical response is highly sensitive to fabrication resolution, especially to the slicing parameter, rather than scanning speed. From the optical microscope images, it could be seen that higher slicing value produced larger and more visible steps, whereas the lower slicing value of 0.05 μm produced a finer staircase approximation with smaller step height, but it resulted in more radial lines. From the camera images, the vortex-like intensity distribution appears to be better defined for the SPPs produced with the lower slicing value rather than with ones fabricated with decreased scanning speed.

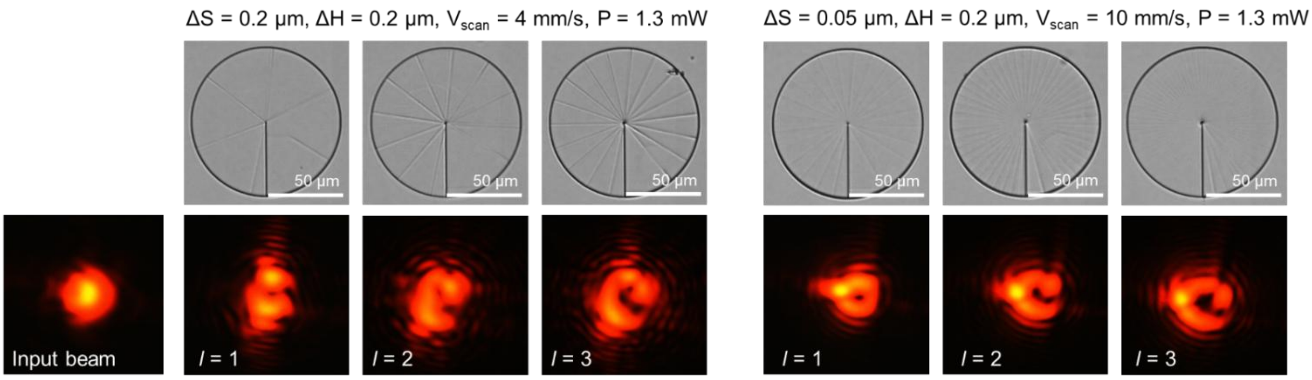

Fig. 35 Top - MPL fabricated SPPs with different printing parameters, bottom – optical performance results at 633 nm.

4.6 Integrated micro-optical devices

As a proof of concept demonstrating the capability of MPL to fabricate complex, miniaturized optical systems, an integrated optical device consisting of a beam expander and a spiral phase plate was designed and fabricated. The structure consisted of BE with a theoretical expansion ratio of 10 and a SPP on top (diameter d = 100 µm, topological charge l = 2). A 10 µm outer margin was intentionally included in the SPP design to ensure the phase modulating area remained intact by the support structures, allowing for simultaneous beam expansion and phase modulation within a single, compact micro-optical element. Finally, scanning electron microscopy confirmed the successful fabrication of this multi-lens architecture, having total height of 138 µm, and the precise realization of the SPP with its characteristic phase step. (Fig. 36)

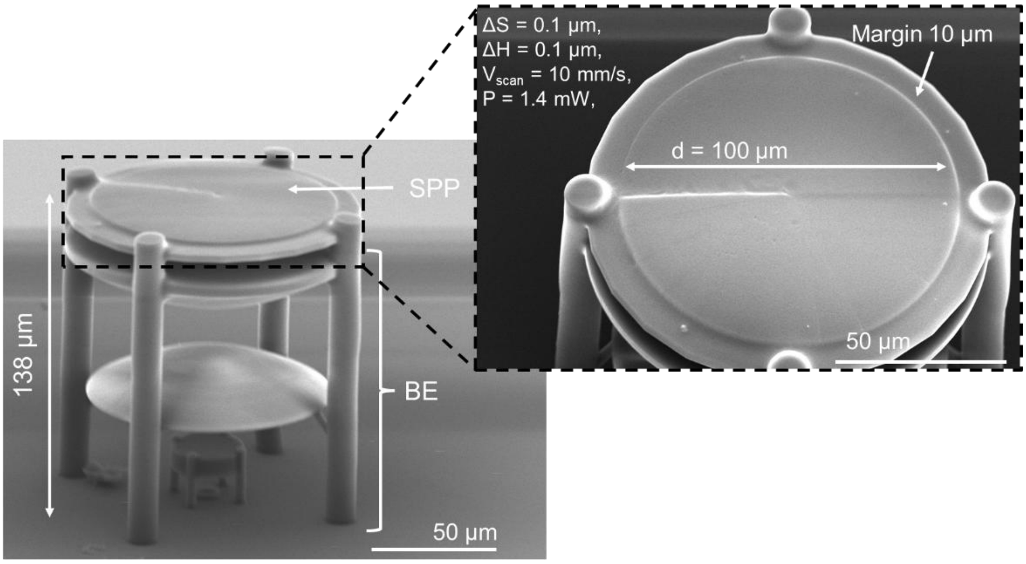

Fig. 36 MPL fabricated compact beam shaping device.

The optical performance of the fabricated micro-device was evaluated using a λ = 633 nm input beam with NA = 0.4, chosen specifically to optimize coupling efficiency into the 10 µm diameter input lens of the BE. After propagation through the beam expander, the beam profile was broadened at an observation plane of z ≈ 600 µm. When the SPP was integrated into the micro-optical device, the output beam retained its expanded spatial footprint but transformed into a characteristic ring-like intensity distribution. (Fig. 37) The normalized intensity cross-section profiles support the generation of a vortex-like beam by showing a characteristic central intensity minimum, which was not observed in the input beam or the BE-only beam. (Fig. 38) This suggests that the integrated BE and SPP architecture modifies the phase of light, generating an optical vortex-like beam and acts as miniaturized beam-shaping device.

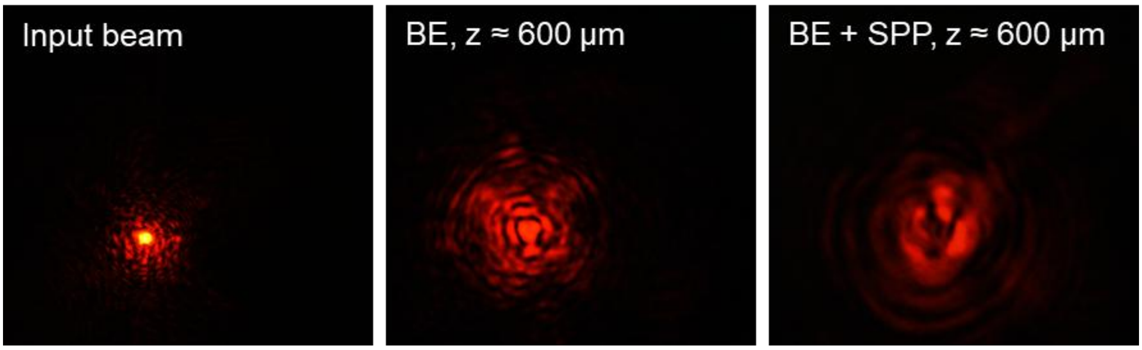

Fig. 37 Optical performance of MPL fabricated beam shaping device.

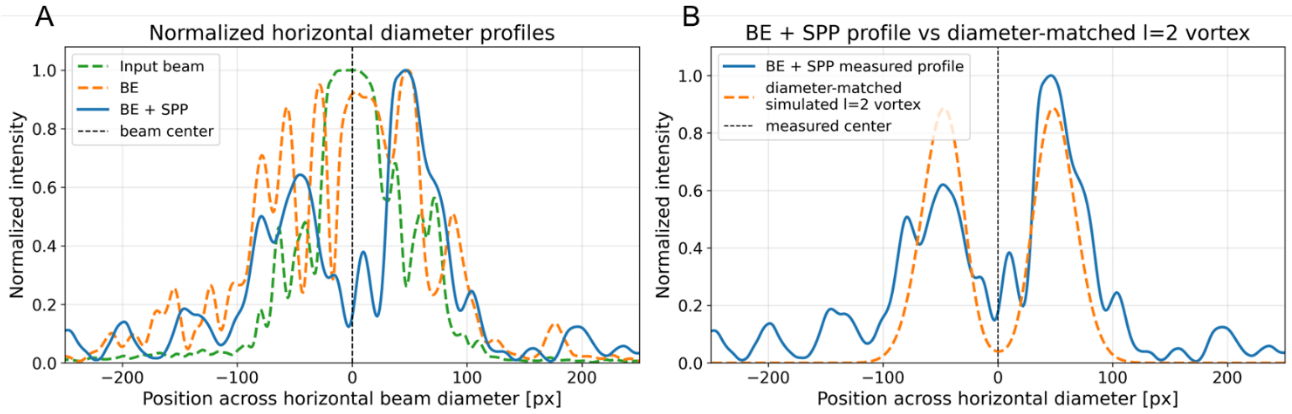

Fig. 38 A – normalized intensity profiles of an input beam and beams passing through BE and beam shaping device. B – comparison of normalized intensity profile of vortex-like beam created by the beam shaping device and diameter-matched simulated vortex-like beam.

5. Discussion

5.1 Strategies to improve light propagation simulations in micro-optics

Light transmission through a 10 μm diameter high-NA lens can produce diffraction patterns or distort the response of the micro-optical element. Therefore, scalar or vector wave-optical simulations are necessary to predict light behavior at microscale and simulate various scenarios such as incomplete illumination, structure tilt, aperture clipping or the influence of opaque platforms or pinhole apertures in integrated micro-optical devices.

Practically, for scalar and vector wave-optical simulations open-source tools such as Diffractio Python package [41] have been used. For example, to simulate light propagation and the focal intensity pattern of a compact diffractive optical element used to analyze the complete polarization state of light, Soria-Garcia et al. [42] used the aforementioned open-source tool. The simulated design identified polarization states with an average uncertainty of 0.006%, and the fabricated device was experimentally validated with an average uncertainty of 3.33%. Similarly, Sanchez-Brea et al. [43] used a Rayleigh–Sommerfeld propagation method implemented in the Diffractio Python package to simulate the focal intensity distribution and depth of focus of angular diffractive lenses, which were later validated experimentally using a spatial light modulator and showed good agreement with the simulations. Ellingen et al. [44] used Diffractio in a scalar Rayleigh–Sommerfeld forward model to simulate far-field diffraction from MPL-printed phase gratings with tilt and curvature errors, originating from substrate holder tilt and objective induced curvature of the focal plane. The simulation of far-field diffraction enabled reconstruction and compensation of printing deviations which were compensated by subtracting a corresponding height map from subsequent print fields.

Important physical phenomena to consider before creating or using scalar and wave-optical tools for simulations are backward reflected fields and light polarization state. Backward reflected fields become important when micro-optical systems contain strong refractive-index discontinuities, multiple interfaces, or shared illumination and detection paths. In such cases, reflected light can interfere with the desired signal. This is particularly relevant for optical fiber-integrated micro-optics and endoscopic probes, where the same optical fiber bundle may be used for illumination and imaging. Wende et al. [45] showed that back-reflected light from imaging fiber facets can overlap with the useful signal and reduce imaging contrast. To model this effect, they introduced a bidirectional wave propagation method, which extends forward wave-propagation simulations by calculating reflected and backward-propagating electric fields. Using this approach, they simulated 3D-printed index-matching caps designed to shift the main reflection away from the fiber facet, enabling suppression of reflected noise and improving the feasibility of compact fiber-based imaging systems. Similarly, it was noticed that scalar propagation models neglect polarization and usually assume that light propagates only in the forward direction. This becomes limiting for high-NA microlenses, where the electric field can no longer be treated as purely scalar and polarization-dependent effects influence focusing, transmission, and reflection at optical interfaces. Wende et al. in recent work [46] addressed this limitation using the fast polarized wave propagation method (FPWPM), which extended scalar simulations to vector electric fields while maintaining practically feasible computation times. This allowed polarization effects to be included in simulations of micro-optical systems such as high-NA microlenses.

However, there is no universal numerical method which can be efficiently applied in all cases. Each method involves approximations and limitations; therefore, the choice of simulation approach should depend on the application and on the relevant physical phenomena. Combining different methods, including ray optics, scalar optics and vector optical simulations allows the system to be evaluated from different perspectives. Although ray tracing is insufficient when diffraction, realistic source-field distributions, or vectorial effects dominate, it can still provide reliable initial designs in cases where its assumptions remain valid. For example, Wende et al. [31] designed 3D-printed immersion micro-optical systems using Zemax ray tracing and subsequently validated the ray tracing designs with FPWPM wave-optical simulations. The wave-optical model confirmed diffraction-limited focusing, and experimental measurements of the fabricated devices also showed diffraction-limited performance, demonstrating that ray tracing can be effective when supported by wave-optical validation and experimental testing.

5.2 Beam expander design and miniaturization performance

Galilean type beam expanders having 5, 7.5, 10 beam expansion ratios and multi-lens beam expanders having 5, 10, 15 beam expansion ratios were designed. For comparison, free-space expansion was estimated for a beam emitted from a 10 µm-core optical fiber using NA = 0.11, corresponding to the specified value for F-SM10 at 1064 nm [47]. This value was used as a conservative upper-bound estimate of beam divergence, since the specified NA near 635 nm is lower, ~0.08. Under the assumption of NA = 0.11, a beam propagating in air would reach diameters of 50 µm, 75 µm, 100 µm, 150 µm in 181 µm, 294 µm, 407 µm, 633 µm distances respectively according to formulas:

$$\theta = arcsin(NA), \tag{19}$$

where θ – half divergence of a beam. Then based on:

$$\theta = arctan(\frac{D_f - D_i}{2L}), \tag{20}$$

we can derive:

$$D_f = D_i + 2L \cdot tan(\theta), \tag{21}$$

where D_i, D_f – beam diameter at initial and final planes respectively, L – axial distance between the planes. [48], [49] By using corresponding Galilean type BEs, such expansion in a modelled system was achieved in 97 µm, 105 µm, 155 µm distances respectively, making the device 1.8 – 2.8 times more compact. And with multi-lens approach corresponding expansion could be achieved in 66 µm, 122 µm, 159 µm giving 2.7 – 4.0 times reduced height of the structure compared to free space light divergence.

Moreover, distributing the optical power of a beam expander over multiple lens elements improves practical beam control by reducing pupil magnification at individual surfaces. When optical power is concentrated in a single lens, the aperture stop is imaged with high magnification, causing rapid growth of marginal-ray heights and increasing the likelihood of vignetting. By spreading optical power across several lenses, the pupil is re-imaged more gradually, leading to smoother marginal ray height evolution along the system and allowing downstream optics to accept the beam without excessively increasing diameter or thickness of downstream optics. [50]

5.3 Optimization of fabrication parameters

When it comes to fabricating BEs, optimization of printing parameters shows that finer slicing and hatching steps lead to improved structural fidelity and surface quality. However, this typically results in substantially longer fabrication times. To mitigate this trade-off, smart slicing and hatching strategies can be employed. To reduce hatching related surface pattern, Zyla et al. [51] demonstrated that replacing a static hatch with an adaptive hatching strategy – using a grid hatch with constant line spacing (0.1 µm) while rotating the grid by 5° after each successive layer, improves both geometric accuracy and surface quality, because each layer better approximates the local circular contour rather than imprinting a repeated directional pattern. In the same work, they combined this with adaptive slicing. They employed region dependent slicing values with 0.1 µm, 0.2 µm, and 0.4 µm distances for assigned to high, moderate, and low fidelity regions of the structure. This could lead to avoiding unnecessary fine discretization in low impact regions therefore having potential to improve printing speed.

In parallel, grayscale (light dose modulated) printing provides a complementary route to smoother optical surfaces by replacing discrete layers with continuous height control. In two-photon grayscale lithography, the laser power is modulated during exposure to generate a controlled polymerization gradient along the beam direction, enabling smooth voxel-size variation within a single written layer yielding continuous variation in height and shape rather than a staircase topography. [52]

Finally, for smart slicing methods aimed to improve surface accuracy without extended print times, Zheng et al. [53] proposed an adaptive direct slicing method based on tilted voxels. In this approach, the parameter is not a fixed slicing distance but the desired overlap between neighboring voxels. Rather than using uniform layers, the algorithm selects a target voxel overlap and computes the local interlayer spacing from the CAD model's contour geometry to maintain that overlap throughout the print. To enable this, voxels are intentionally tilted by steering the laser beam off-axis. They report that the approach reduces layer number by more than 30% and staircase errors decreased significantly.

5.4 Improving optical performance measurements

Intended application of MPL fabricated BEs and integrated micro-optical devices was to modulate the light coming from the core of single-mode optical fiber. Therefore, the design had 10 µm diameter first lens which resembles the core diameter of single-mode optical fibers. [47] During physical testing of MPL fabricated micro-optical elements, one practical limitation was the alignment of the input beam to the 10 µm diameter first lens aperture. The available XY translation stage (8MTF, Standa) had a minimum step size of 2.5 µm, which made accurate centering of the beam difficult. This limitation is particularly important for such small-aperture elements, where even a slight lateral displacement can cause partial illumination, enhanced diffraction resulting in distorted beam profiles.

To tackle this issue either more precise piezoelectric positioner could be integrated together with motor driven mechanical translation stage, or a beam blocker approach could be used. Opaque platforms made with MPL could act as a spatial filter, aperture stop, ensuring that only the intended 10 µm diameter micro-optical aperture remains transparent. Opaque structures fabricated by laser overexposure during MPL process demonstrate that local resin decomposition produces dark regions that block transmitted light. Nair et al. [54] used this approach to fabricate opaque and transparent regions from a single resin and demonstrated an opaque aperture integrated with a transparent lens. (Fig. 39)

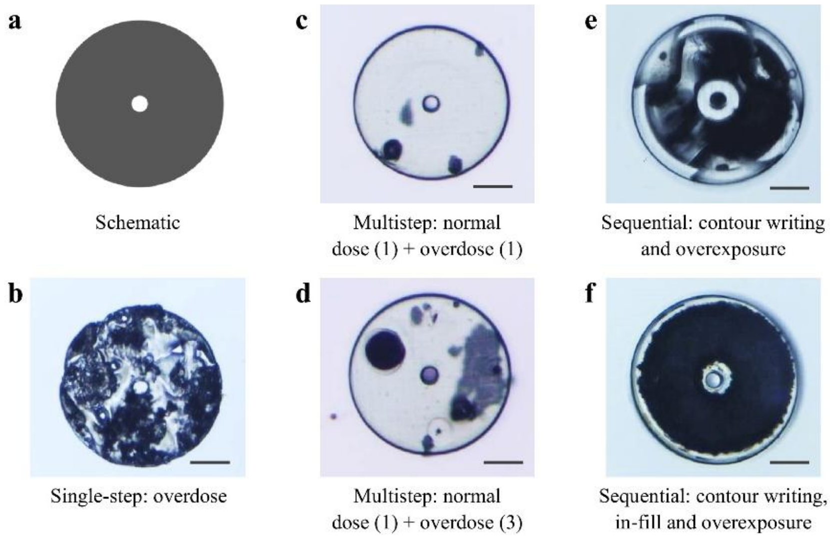

Fig. 39 Fabrication processes to achieve opacity. a – pinhole design, b – structure obtained with a single-step laser exposure under overdose conditions, c – structure fabricated through multistep exposure: first exposure with normal dose and second exposure with overdose, d – structure fabricated through

multistep exposure: exposure with normal dose followed by overdose exposure of the same area for three cycles, e – pinhole fabricated with sequential exposure (contour written first and inner areas overexposed next), and f – pinhole fabricated with sequential exposure (contour writing followed by in-fill fabrication in inner areas and overexposure of the inner areas). Scalebar: 50 µm. [54]

Although opaque MPL structures can be produced by laser-induced decomposition of the resin, direct overexposure is difficult to control because local heating produces bubbles, structural damage and non-uniform opacity as discussed in Section 2.1. An alternative approach is to incorporate a highly absorptive black photoresist into the MPL process. Schmid et al. [55] demonstrated IP-Black, an epoxy-based photoresist that exhibits strong absorption in the visible spectral range, particularly between 450 nm and 650 nm, where 250 µm thick printed regions transmit less than 5% of incident light. At the same time, the photoresist remains sufficiently transmissive at the 780 nm writing wavelength to allow multiphoton polymerization.

5.5 Enhancing optical transmission of MPL printed micro-optics

In the present work, the structure with the highest number of refractive interfaces showed a measured transmission of approximately 69% relative to the glass substrate. It slightly deviated from theoretical estimations based only on Fresnel reflections, suggesting that additional loss mechanisms contribute to the measured light attenuation. These may include scattering from surface roughness, deviations from the designed geometry, and internal refractive-index variations caused by incomplete polymerization or local differences in cross-linking density. Therefore, post-processing strategies that densify the material and improve the homogeneity of the refractive-index distribution could potentially improve optical performance. SZ2080^{TM} photoresist could enable highly transmissive properties of the structures for visible and IR spectrum as it has inorganic part, which could be revealed by removing organic components from the material. [36] In this case calcination of SZ2080^{TM} could be used to remove the organic part and densify the inorganic network, resulting in structures that are optically transparent and mechanically robust. [56] Similar approach is presented in Gailevičius et al. works. [57] Here after printing, SZ2080^{TM} structures were annealed (heated to ~1000–1500 °C) to burn out organic content. The result is inorganic microstructure with greatly enhanced thermal and chemical robustness and optical transparency as it is zirconia/silica-based inorganic microstructure. However, Gonzalez-Hernandez et al. [56] similarly 3D-printed SZ2080^{TM} structures and found that 50 µm-diameter SZ2080^{TM} lens isotropically shrinks by ~40% after calcination at 1100 °C. The shrinkage should be carefully considered before calcination. This could be addressed by compensating model dimensions before printing or by tailoring the prepolymer composition, since it has been shown that the magnitude of shrinkage in hybrid materials depends on the relative ratios of the organic and inorganic components as higher shrinkage is observed for formulations with a larger organic fraction. [58]

In addition, resin formulations targeting post-processing and high optical transparency deliberately avoid the use of photoinitiators. As demonstrated for the hybrid organic–inorganic photoresist SZ2080™, photoinitiators are not eliminated during polymerization or moderate heat treatment but remain embedded in the final structure as residual molecules, leading to increased autofluorescence. Ladika et al. [59] showed that structures fabricated from non-photosensitized SZ2080™ exhibit fluorescence intensities nearly an order of magnitude lower than photoinitiator containing counterparts. Only high-temperature pyrolysis, which removes the entire organic fraction and converts the material into a glass-ceramic, can fully eliminate photoinitiator-derived species, however, this process fundamentally alters the material and induces substantial shrinkage. [60] Therefore, for applications requiring optical clarity, PI-free resin formulations are preferred.

Although the measured transmission in the present work was slightly lower than the Fresnel reflection estimate, the overall transmission trend followed the number of refractive interfaces. This suggests that cumulative Fresnel reflections are the dominant baseline loss mechanism. Consequently, as a solution to increase light transmission, anti-reflective (AR) coatings deposited by atomic layer deposition (ALD) technology can be applied to increase transmission for multi-element micro-optical systems. Astrauskytė et al. [61] observed that anti-reflective coating (23 nm titanium oxide and 130.8 nm aluminum oxide layers) deposited via ALD decreased the reflection from 3.3% to 0.1% at a wavelength of 633 nm for one surface of SZ2080™. Also, imaging through AR coated microlenses, had negligible changes in image quality, which is a promising result in the pursuit to fabricate supporting structures for light structuring optical elements. However, changes in the microlens focal lengths which correlate with the changes in the microlens height were noticed. In the case of aluminum oxide, focal length decreased by 7.5–8% after deposition and increased by 2–7% after TiO_2 deposition.

6. Conclusions

1. Under the design constraints of a 10 µm input beam diameter and a lateral lens size below 200 µm, the multi-lens architecture outperformed the classical Galilean design in geometrical-optics performance, achieving 100% geometrical transmission by reducing vignetting and enabling greater beam expansion ratios while minimizing overall structure height, making it more suitable for fabrication with high-NA objectives to maintain feature fidelity.
2. MPL-fabricated beam expander (M = 10) broadens the incident 633 nm beam while it propagates inside the microlens, followed by reduced downstream divergence, achieving a 1.8 times smaller beam diameter at a 6 cm distance relative to free-space propagation.
3. MPL-fabricated SPPs generated vortex-like intensity distributions for $l = 1$, $l = 2$, and $l = 3$ at 633 nm, with a central intensity minimum that increased with topological charge, making them suitable for beam-shaping applications.
4. MPL enables precise fabrication of beam-shaping elements and micro-optics and allows their integration within compact (~138 µm) micro-optical devices for complex optical functionalities in a single micro-architecture achieving ~3 times smaller footprint compared with existing micro-optical approaches.

References

[1] D. Gonzalez-Hernandez, S. Varapnickas, A. Bertoncini, C. Liberale, and M. Malinauskas, “Micro-Optics 3D Printed via Multi-Photon Laser Lithography,” *Advanced Optical Materials*, vol. 11, no. 1, p. 2201701, 2023, doi: 10.1002/adom.202201701.

[2] V. R. Manfrinato *et al.*, “Resolution Limits of Electron-Beam Lithography toward the Atomic Scale,” *Nano Lett.*, vol. 13, no. 4, pp. 1555–1558, Apr. 2013, doi: 10.1021/nl304715p.

[3] J. Fischer and M. Wegener, “Three-dimensional optical laser lithography beyond the diffraction limit,” *Laser & Photonics Reviews*, vol. 7, no. 1, pp. 22–44, 2013, doi: 10.1002/lpor.201100046.

[4] Q. Zhang *et al.*, “Diffractive optical elements 75 years on: from micro-optics to metasurfaces,” *PI*, vol. 2, no. 4, p. R09, Dec. 2023, doi: 10.3788/PI.2023.R09.

[5] Y. Wang *et al.*, “Ultra-compact visible light depolarizer based on dielectric metasurface,” *Appl. Phys. Lett.*, vol. 116, no. 5, p. 051103, Feb. 2020, doi: 10.1063/1.5133006.

[6] C. Li *et al.*, “Metafiber transforming arbitrarily structured light,” *Nat Commun*, vol. 14, no. 1, p. 7222, Nov. 2023, doi: 10.1038/s41467-023-43068-7.

[7] J. E. Fröch *et al.*, “Real time full-color imaging in a Meta-optical fiber endoscope,” *eLight*, vol. 3, no. 1, p. 13, Jun. 2023, doi: 10.1186/s43593-023-00044-4.

[8] D. K. Sugioka, D. Y. Hanada, and D. K. Midorikawa, “3D microchips fabricated by femtosecond laser for biomedical applications,” in *Optomechatronic Technologies 2008*, SPIE, Nov. 2008, p. 23. doi: 10.1117/12.817357.

[9] E. Skliutas *et al.*, “Polymerization mechanisms initiated by spatio-temporally confined light,” *Nanophotonics*, vol. 10, no. 4, pp. 1211–1242, 2021, doi: 10.1515/nanoph-2020-0551.

[10] M. Lebedevaite, J. Ostrauskaite, E. Skliutas, and M. Malinauskas, “Photoinitiator Free Resins Composed of Plant-Derived Monomers for the Optical µ-3D Printing of Thermosets,” *Polymers (Basel)*, vol. 11, no. 1, p. 116, Jan. 2019, doi: 10.3390/polym11010116.

[11] Y. Bougdid and Z. Sekkat, “Voxels Optimization in 3D Laser Nanoprinting,” *Sci Rep*, vol. 10, no. 1, p. 10409, Jun. 2020, doi: 10.1038/s41598-020-67184-2.

[12] G. Zyla and M. Farsari, “Frontiers of Laser-Based 3D Printing: A Perspective on Multi-Photon Lithography,” *Laser & Photonics Reviews*, vol. 18, no. 7, p. 2301312, 2024, doi: 10.1002/lpor.202301312.

[13] D. Samsonas *et al.*, “3D nanopolymerization and damage threshold dependence on laser wavelength and pulse duration,” *Nanophotonics*, vol. 12, no. 8, pp. 1537–1548, doi: 10.1515/nanoph-2022-0629.

[14] D. Gailevicius, R. Zvirblis, K. Galvanauskas, G. Bataviciute, and M. Malinauskas, “Calcination-Enhanced Laser-Induced Damage Threshold of 3D Micro-Optics Made with Laser Multi-Photon Lithography,” *Photonics*, vol. 10, no. 5, May 2023, doi: 10.3390/photonics10050597.

[15] S. Ristok, P. Flad, and H. Giessen, “Atomic layer deposition of conformal anti-reflective coatings on complex 3D printed micro-optical systems,” *Opt. Mater. Express, OME*, vol. 12, no. 5, pp. 2063–2071, May 2022, doi: 10.1364/OME.454475.

[16] F. Träger, Ed., *Springer Handbook of Lasers and Optics*. in Springer Handbooks. Berlin, Heidelberg: Springer, 2012. doi: 10.1007/978-3-642-19409-2.

[17] X. Luo, *Engineering Optics 2.0: A Revolution in Optical Theories, Materials, Devices and Systems*. Singapore: Springer, 2019. doi: 10.1007/978-981-13-5755-8.

[18] M. W. Beijersbergen, R. P. C. Coerwinkel, M. Kristensen, and J. P. Woerdman, “Helical-wavefront laser beams produced with a spiral phaseplate,” *Optics Communications*, vol. 112, no. 5, pp. 321–327, Dec. 1994, doi: 10.1016/0030-4018(94)90638-6.

[19] A. A. Paraipan *et al.*, “Scanless Spectral Imaging of Terahertz Vortex Beams Generated by High-Resolution 3D-Printed Spiral Phase Plates,” *Small Science*, vol. 4, no. 12, p. 2400352, 2024, doi: 10.1002/smsc.202400352.

[20] E. Brasselet, M. Malinauskas, A. Žukauskas, and S. Juodkazis, “Photopolymerized microscopic vortex beam generators: Precise delivery of optical orbital angular momentum,” *Appl. Phys. Lett.*, vol. 97, no. 21, p. 211108, Nov. 2010, doi: 10.1063/1.3517519.

[21] J. Ni *et al.*, “Three-dimensional chiral microstructures fabricated by structured optical vortices in isotropic material,” *Light Sci Appl*, vol. 6, no. 7, pp. e17011–e17011, Jul. 2017, doi: 10.1038/lsa.2017.11.

[22] I. V. A. K. Reddy, A. Bertoncini, and C. Liberale, “3D-printed fiber-based zeroth- and high-order Bessel beam generator,” *Optica, OPTICA*, vol. 9, no. 6, pp. 645–651, Jun. 2022, doi: 10.1364/OPTICA.453839.

[23] “3D-printed eagle eye: Compound microlens system for foveated imaging.” Accessed: May 20, 2026. [Online]. Available: https://www.science.org/doi/10.1126/sciadv.1602655

[24] J. Liu, R. Lycke, L. Luan, and T. S. Tkaczyk, “Fully 3D-printed endomicroscopic objective for two-photon, multi-wavelength excitation microscopy,” *Biomed Opt Express*, vol. 17, no. 1, pp. 82–97, Dec. 2025, doi: 10.1364/BOE.579476.

[25] T. Gissibl, S. Thiele, A. Herkommer, and H. Giessen, “Two-photon direct laser writing of ultracompact multi-lens objectives,” *Nature Photon*, vol. 10, no. 8, pp. 554–560, Aug. 2016, doi: 10.1038/nphoton.2016.121.

[26] “Thorlabs · Beam Expander Design Comparison: Keplerian and Galilean.” Accessed: May 20, 2026. [Online]. Available: https://www.thorlabs.com/beam-expander-design-comparison-keplerian-and-galilean?tabName=Insights

[27] H. Wang, H. Wang, W. Zhang, and J. K. W. Yang, “Toward Near-Perfect Diffractive Optical Elements via Nanoscale 3D Printing,” *ACS Nano*, vol. 14, no. 8, pp. 10452–10461, Aug. 2020, doi: 10.1021/acsnano.0c04313.

[28] W. J. Smith, *Optical engineering: the design of optical systems*, 4. ed. New York: McGraw-Hill, 2008.

[29] "Multi-material multi-photon 3D laser micro- and nanoprinting." Accessed: Jan. 21, 2026. [Online]. Available: https://www.light-am.com/article/doi/10.37188/lam.2021.017

[30] M. Schmid, S. Thiele, A. Herkommer, and H. Giessen, "Three-dimensional direct laser written achromatic axicons and multi-component microlenses," *Opt. Lett., OL*, vol. 43, no. 23, pp. 5837–5840, Dec. 2018, doi: 10.1364/OL.43.005837.

[31] M. Wende, K. Doth, M. Heymann, and A. Toulouse, "3D-printed immersion micro optics," *gxjzz*, vol. 6, no. 2, pp. 388–394, Jul. 2025, doi: 10.37188/lam.2025.019.

[32] D. C. O'Shea and A. Zajac, "*Elements of Modern Optical Design*," *Physics Today*, vol. 39, no. 5, pp. 87–88, May 1986, doi: 10.1063/1.2815008.

[33] N. Lindlein, "Simulation of micro-optical systems including microlens arrays," *J. Opt. A: Pure Appl. Opt.*, vol. 4, no. 4, p. S1, Jul. 2002, doi: 10.1088/1464-4258/4/4/351.

[34] M. Wende, J. Drozella, A. Toulouse, and A. M. Herkommer, "Fast algorithm for the simulation of 3D-printed microoptics based on the vector wave propagation method," *Opt. Express, OE*, vol. 30, no. 22, pp. 40161–40173, Oct. 2022, doi: 10.1364/OE.469178.

[35] D. B. Murphy and M. W. Davidson, *Fundamentals of light microscopy and electronic imaging*, 2nd ed. Hoboken, N.J: Wiley-Blackwell, 2013.

[36] "Ultra-Low Shrinkage Hybrid Photosensitive Material for Two-Photon Polymerization Microfabrication | ACS Nano." Accessed: Jan. 21, 2026. [Online]. Available: https://pubs.acs.org/doi/10.1021/nn800451w

[37] M. Stavrou *et al.*, "Direct measurement of two-photon absorption and refraction properties of SZ2080TM-based resists at 515 nm: insights into 3D printing," *Nanophotonics*, vol. 14, no. 18, pp. 2981–2992, Sep. 2025, doi: 10.1515/nanoph-2025-0066.

[38] "EVIDENT OLS5100 INSTRUCTIONS MANUAL Pdf Download," ManualsLib. Accessed: Jan. 21, 2026. [Online]. Available: https://www.manualslib.com/manual/3736279/Evident-Ols5100.html

[39] "Balluff - BVS CA-MLC / BVS CA-IGC / mvBlueFOX Technical Documentation: Introduction." Accessed: May 20, 2026. [Online]. Available: https://assets.balluff.com/MV_Manuals/online/mvBlueFOX/mvBF_page_introduction.html

[40] "Balluff - BVS CA-MLC / BVS CA-IGC / mvBlueFOX Technical Documentation: mvBlueFOX-[Model]223 (1.4 Mpix [1360 x 1024])." Accessed: May 20, 2026. [Online]. Available: https://assets.balluff.com/MV_Manuals/online/mvBlueFOX/CCD1360_section_1_1.html

[41] *diffractio: Optical Diffraction and Interference (scalar and vectorial)*. Python. Accessed: May 20, 2026. [Online]. Available: https://github.com/optbrea/diffractio

[42] A. Soria-Garcia *et al.*, "Vector diffractive optical element as a full-Stokes analyzer," *Optics & Laser Technology*, vol. 163, p. 109400, Aug. 2023, doi: 10.1016/j.optlastec.2023.109400.

[43] L. M. Sanchez-Brea, F. J. Torcal-Milla, J. del Hoyo, A. Cuadrado, and J. A. Gomez-Pedrero, "Optimization of angular diffractive lenses with extended depth of focus," *J. Opt.*, vol. 22, no. 6, p. 065601, Apr. 2020, doi: 10.1088/2040-8986/ab8614.

[44] E. Ellingen, M. Rohde, B. Stahl, and R. Lange, "Fourier scatterometry for compensation of tilt and curvature deviations of two-photon polymerization three-dimensional printers," *JOM*, vol. 3, no. 4, p. 043501, Nov. 2023, doi: 10.1117/1.JOM.3.4.043501.

[45] M. Wende, J. Drozella, and A. M. Herkommer, "Fast bidirectional vector wave propagation method showcased on targeted noise reduction in imaging fiber bundles using 3D-printed micro optics," *Opt. Express, OE*, vol. 31, no. 18, pp. 28874–28890, Aug. 2023, doi: 10.1364/OE.497244.

[46] M. Wende, J. Drozella, A. Toulouse, and A. M. Herkommer, "Fast vector wave optical simulation methods for application on 3D-printed microoptics," *JOM*, vol. 4, no. 2, p. 024501, Apr. 2024, doi: 10.1117/1.JOM.4.2.024501.

[47] "F-SM10 Photonic Crystal Fiber." Accessed: May 20, 2026. [Online]. Available: https://www.newport.com/p/F-SM10

[48] F. Mitschke, *Fiber Optics*. Berlin, Heidelberg: Springer Berlin Heidelberg, 2010. doi: 10.1007/978-3-642-03703-0.

[49] "Microsoft Word - C033626e.doc." Accessed: Jan. 21, 2026. [Online]. Available: https://lab.semi.ac.cn/download/0.09758513607615016.pdf

[50] D. C. O'Shea, *Elements of modern optical design*, 6. Dr. in Wiley Series in pure and applied optics. New York: Wiley, 1985.

[51] G. Zyla *et al.*, "3D micro-devices for enhancing the lateral resolution in optical microscopy," *gxjzz*, vol. 5, no. 2, pp. 204–217, Aug. 2024, doi: 10.37188/lam.2024.019.

[52] J. Lu, X. W. Ng, D. Piston, and T. S. Tkaczyk, "Fabrication of a multifaceted mapping mirror using two-photon polymerization for a snapshot image mapping spectrometer," *Appl Opt*, vol. 62, no. 20, pp. 5416–5426, Jul. 2023, doi: 10.1364/AO.495466.

[53] X. Zheng, K. Cheng, X. Zhou, J. Lin, and X. Jing, "An adaptive direct slicing method based on tilted voxel of two-photon polymerization," *Int J Adv Manuf Technol*, vol. 96, no. 1, pp. 521–530, Apr. 2018, doi: 10.1007/s00170-017-1507-3.

[54] "Fabrication of opaque and transparent 3D structures using a single material via two-photon polymerisation lithography." Accessed: May 20, 2026. [Online]. Available: https://www.light-am.com/en/article/doi/10.37188/lam.2023.025

[55] M. D. Schmid, A. Toulouse, S. Thiele, S. Mangold, A. M. Herkommer, and H. Giessen, "3D Direct Laser Writing of Highly Absorptive Photoresist for Miniature Optical Apertures," *Advanced Functional Materials*, vol. 33, no. 39, p. 2211159, 2023, doi: 10.1002/adfm.202211159.

[56] D. Gonzalez-Hernandez *et al.*, "Laser 3D Printing of Inorganic Free-Form Micro-Optics," *Photonics*, vol. 8, no. 12, Dec. 2021, doi: 10.3390/photonics8120577.

[57] D. Gailevičius, V. Padolskytė, L. Mikoliūnaitė, S. Šakirzanovas, S. Juodkazis, and M. Malinauskas, “Additive-manufacturing of 3D glass-ceramics down to nanoscale resolution,” *Nanoscale Horizons*, vol. 4, no. 3, pp. 647–651, 2019, doi: 10.1039/C8NH00293B.

[58] “Laser additive manufacturing of Si/ZrO2 tunable crystalline phase 3D nanostructures.” Accessed: Jan. 21, 2026. [Online]. Available: https://www.oejournal.org/oea/article/doi/10.29026/oea.2022.210077

[59] D. Ladika *et al.*, “X-photon 3D lithography by fs-oscillators: wavelength-independent and photoinitiator-free,” *gxjzz*, vol. 5, no. 4, pp. 567–579, Jan. 2025, doi: 10.37188/lam.2024.048.

[60] L. Jonušauskas *et al.*, “Optically Clear and Resilient Free-Form µ-Optics 3D-Printed via Ultrafast Laser Lithography,” *Materials*, vol. 10, no. 1, Jan. 2017, doi: 10.3390/ma10010012.

[61] D. Astrauskytė, K. Galvanauskas, D. Gailevičius, M. Drazdys, M. Malinauskas, and L. Grineviciute, “Anti-Reflective Coatings Produced via Atomic Layer Deposition for Hybrid Polymer 3D Micro-Optics,” *Nanomaterials*, vol. 13, no. 16, Aug. 2023, doi: 10.3390/nano13162281.

Summary

Over recent years, the field of modern optics exploiting free-form optics and flat optics such as metasurfaces at the microscale has attracted increasing research interest. This grow is driven by the aim to miniaturize optical elements and enhance overall compactness of optical systems while maintaining effective control of light through integrated designs. Within this context, one of the key technologies enabling fabrication of miniaturized optics is multi-photon lithography (MPL) – a maskless 3D lithography technique which, in combination with highly transparent photoresist, allows the realization of free-form micro-optical elements. At present, the practical extent to which micro-optical systems can be scaled down while still satisfying the assumptions of wave optics and the constraints imposed by MPL remains an open question. For instance, existing integrated optics designs report system lengths of several hundred micrometers to achieve sufficient beam diameter for effective light modulation. To explore the feasibility of further reducing the size of micro-optical system designs, this work investigates MPL fabricated micro beam expanders realized using an organic-inorganic hybrid photoresist – SZ2080^{TM}, which enables the fabrication of accurate three-dimensional structures with high fidelity. Initial designs of Galilean type beam expanders showed a 2.5-fold more compact arrangement compared with existing optical fiber-integrated light-shaping devices. The multi-lens configuration further decreased the height of the micro-optical device and thus supported larger beam expansion ratios while remaining compatible with high-NA MPL fabrication. Optical performance assessment showed that the MPL-fabricated beam expander reduces beam divergence by a factor of 1.8 after 6 cm of propagation compared with free-space propagation, whereas MPL-fabricated spiral phase plates produced characteristic vortex-like intensity distributions, demonstrating their suitability for beam-shaping applications. The combined micro-optical device, consisting of a beam expander and a spiral phase plate within a total height of 138 μm, also showed a vortex-like intensity distribution, suggesting that MPL can integrate complex optical functionalities within a single micro-architecture.

Santrauka

Pastaraisiais metais vis didesnį susidomėjimą kelia šiuolaikinės optikos sritis, kurioje naudojama laisvos formos optika ir plokščiosios optikos elementai, pavyzdžiui, metapaviršiai. Šį susidomėjimą skatina siekis mažinti optinius elementus ir padidinti bendrą optinių sistemų kompaktiškumą, tuo pačiu išlaikant veiksmingą šviesos valdymą integruotose konstrukcijose. Šiame kontekste viena iš pagrindinių technologijų, leidžiančių gaminti miniatiūrinius optinius elementus, yra daugiafotonė litografija (*angl.* multi-photon lithography – MPL). Tai yra trimatės litografijos technika, kuri, kartu su skaidria derva, nenaudojant kaukių, leidžia sukurti laisvos formos mikrooptinius elementus. Šiuo metu klausimas, kokiu mastu praktiškai įmanoma sumažinti mikrooptines sistemas, kad jos atitiktų banginės optikos prielaidas ir tenkintų MPL keliamus apribojimus, išlieka atviras. Pavyzdžiui, esamų integruotos optikos tyrimų duomenimis, norint pasiekti pakankamą spindulio skersmenį veiksmingam šviesos moduliavimui, sistemos ilgis siekia kelis šimtus mikrometrų. Siekiant dar labiau sumažinti mikrooptinių sistemų dydį, šiame darbe tiriami MPL pagaminti šviesos pluošto mikroplėtikliai, sukurti naudojant hibridinę organinę-neorganinę fotodervą – SZ2080^{TM}, kuri leidžia gaminti trimatės struktūras aukštu tikslumu. Pradiniai Galilėjaus tipo pluošto plėtiklių modeliai parodė 2,5 karto kompaktiškesnę konfigūraciją, palyginti su esamais modeliais, skirtais optinio pluošto moduliavimui. Daugialęšė pluošto plėtiklių konfigūracija dar labiau sumažino mikrooptinio prietaiso matmenis, todėl buvo galima pasiekti didesnius spindulio išplėtimo koeficientus, tuo pačiu išlaikant suderinamumą su didelės skaitinės apertūros objektyvais, naudojamais MPL gamyboje. Optiniai eksperimentai parodė, kad MPL pagamintas spindulio plėtiklis 6 cm pluošto sklidimo atstumu sumažina spindulių skėstį 1,8 karto, lyginant su pluošto sklidimu ore, o MPL pagamintos spiralinės fazinės plokštelės formavo būdingus sūkurio formos intensyvumo pasiskirstymus, įrodydamos savo tinkamumą šviesos moduliavimo taikymams. Integruotas mikrooptinis įrenginys, susidedantis iš pluošto plėtiklio ir spiralinės fazinės plokštelės, kurio bendras aukštis siekė 138 µm, taip pat formavo sūkurio formos intensyvumo pasiskirstymą, o tai rodo, kad, naudojant daugiafotonę litografiją, kompleksiniai optiniai funkcionalumai gali būti pasiekti vienoje kompaktiškoje mikrooptinėje architektūroje.